

Banner appropriate to article type will appear here in typeset article

Surface reflection of bottom generated oceanic lee waves

L. E. Baker¹†, and A. Mashayek¹

¹Department of Civil and Environmental Engineering, Imperial College London

(Received xx; revised xx; accepted xx)

Lee waves generated by stratified flow over rough bottom topography in the ocean extract momentum and energy from the geostrophic flow, causing drag and enhancing turbulence and mixing in the interior ocean when they break. Inviscid linear theory is generally used to predict the generation rate of lee waves, but the location and mechanism of wave breaking leading to eventual dissipation of energy and irreversible mixing are poorly constrained. In this study, a linear model with viscosity, diffusivity, and an upper boundary is used to demonstrate the potential importance of the surface in reflecting lee wave energy back into the interior, making the case for treating lee waves as a full water column process. In the absence of critical levels, it is shown that lee waves can be expected to interact with the upper ocean, resulting in enhanced vertical velocities and dissipation and mixing near the surface. The impact of the typical oceanic conditions of increasing background velocity and stratification with height above bottom are investigated and shown to contribute to enhanced upper ocean vertical velocities and mixing.

1. Introduction

Oceanic lee waves are quasi-steady internal gravity waves generated by the interaction of geostrophic flows with submarine topography. They are present throughout the world's oceans, accounting for an estimated 0.2 - 0.75 TW of conversion from the geostrophic flow (Scott *et al.* 2011; Nikurashin & Ferrari 2011; Wright *et al.* 2014). Approximately half of this generation takes place in the Southern Ocean (SO) (Nikurashin & Ferrari 2011), where lee waves have been shown to be an important sink of energy and momentum from the energetic mesoscale eddies of the Antarctic Circumpolar Current (ACC) due to the rough topography and high bottom velocities in the region (Nikurashin & Ferrari 2010*b*; Nikurashin *et al.* 2012; Naveira Garabato *et al.* 2013; Yang *et al.* 2018).

Lee waves play an important role not only in the momentum budget of the mean flow through lee wave drag, but also in the buoyancy and tracer budgets through diapycnal mixing. Enhanced levels of turbulence above topography associated with lee waves and other topographic interaction processes are an important source of diapycnal mixing in the deep ocean, contributing to the closure of the meridional overturning circulation (MOC) (MacKinnon *et al.* 2017; Cessi 2019; Cimoli *et al.* 2021). The Southern Ocean upwelling of tracers such as CO₂ and nutrients for primary production are also sensitive to mixing in the

† Email address for correspondence: l.baker18@imperial.ac.uk

36 ocean, with important consequences for air-sea fluxes and ultimately climate (Talley *et al.*
37 2016).

38 Lee wave horizontal lengthscales are typically of order 500 m - 10 km in the ocean, a range
39 that is unresolved in global climate models, so the mixing and drag effects of lee waves
40 both need to be parametrised. The generation of lee waves is usually understood using linear
41 theory, whereby the lee wave perturbations are assumed to have a much smaller amplitude
42 than the mean flow itself (Bell 1975). An important parameter determining the linearity of lee
43 waves generated at topography of characteristic height h in uniform background stratification
44 N and flow speed U is the lee wave Froude number $Fr_L = Nh/U$ (Mayer & Fringer 2017).
45 Lee waves can propagate vertically when their horizontal wavenumber k (set by topography)
46 is such that $|f| < |Uk| < |N|$, where f is the Coriolis parameter. Under the assumption
47 $|f| \ll |Uk| \ll |N|$, Fr_L is proportional to the ratio of the topographic height h to the lee
48 wave vertical wavelength, or equivalently the ratio of the perturbation horizontal velocity to
49 the background velocity, thus the linear approximation is formally valid for $Fr_L \ll 1$. Energy
50 flux calculated using the linear approximation has been shown to agree with two-dimensional
51 (2D) nonlinear simulations for $Fr_L \lesssim O(1)$ (Nikurashin *et al.* 2014).

52 For 2D topography and flow conditions such that Fr_L is greater than some critical Froude
53 number $Fr_L^{\text{crit}} \sim O(1)$, topographic blocking occurs since the flow lacks the kinetic energy
54 to raise itself over a bump of height greater than $\sim U/N$ (Smith 1989). Thus, the effective
55 height of topography h^{eff} is always reduced such that the waves are generated with $Fr_L^{\text{eff}} =$
56 $Nh^{\text{eff}}/U \lesssim Fr_L^{\text{crit}}$ (Winters & Armi 2012). When the topography is three dimensional (3D),
57 splitting may also occur as the flow goes around rather than over a bump, and the effective
58 height is lower still. Nikurashin *et al.* (2014) found that for multichromatic topography with
59 h defined as the RMS (root mean square) topographic height, $Fr_L^{\text{crit}} \simeq 0.7$ for 2D topography,
60 and $Fr_L^{\text{crit}} \simeq 0.4$ for 3D topography. Thus, with modifications for finite amplitude and 3D
61 effects, the linear theory can be used with some success even when the RMS topographic
62 height violates the linear approximation. Several estimates of energy conversion from the
63 geostrophic flow to lee waves have been found using estimated topographic spectra, bottom
64 velocities and stratification globally (Bell 1975; Scott *et al.* 2011; Nikurashin & Ferrari 2011;
65 Wright *et al.* 2014). Problems remain with this approach, such as the proper representation
66 of blocking in the topographic spectrum, and the neglect of the influence of flow due to large
67 scale topography on the radiating lee waves, which can significantly impact the dissipation
68 above topography (Klymak 2018).

69 Although the generation of lee waves is well understood in a linear sense, the ultimate fate of
70 lee wave energy as a fundamentally nonlinear and dissipative process is poorly constrained.
71 After generation, lee waves radiate vertically and downstream away from topography. A
72 vertical structure function exponentially decreasing with height above bottom was proposed
73 by St. Laurent *et al.* (2002) for parametrisation of the dissipation rate due to the breaking
74 of internal tides, and this has been implemented in lee wave parametrisations with decay
75 scales between 300 and 1000 m (Nikurashin & Ferrari 2013; Melet *et al.* 2014). Both of
76 these studies found that water mass transformation was sensitive to the decay scale used, thus
77 accurate parametrisation of the vertical structure of mixing and dissipation is necessary for
78 correctly predicting the ocean state in global climate models.

79 Lee waves also play an important role in causing drag on the flow, especially in the ACC
80 (Naveira Garabato *et al.* 2013; Yang *et al.* 2018). When flow impinges on topography, the
81 pressure differences across the topographic features cause drag, known as form drag. If there
82 is topographic blocking, or the conditions for radiation of lee waves are not met, this drag
83 will force the flow local to the topography. However, if lee waves are generated and propagate
84 upwards this drag is distributed across the water column as a wave drag, locally forcing the

85 flow where the waves break. Thus, the vertical distribution of the decelerating force on the
 86 mean flow due to lee wave breaking must also be parametrised. In the linear theory, the
 87 energy flux at topography is equal to the product of the total lee wave drag and the bottom
 88 background velocity, but the vertical distributions of the forcing on the flow and the energy
 89 loss need not be the same.

90 Possible sinks for lee wave energy include breaking due to vertical shear from inertial
 91 oscillations generated by parametric instability (Nikurashin & Ferrari 2010a), dissipation
 92 at critical levels (Booker & Bretherton 1967), breaking due to convective instability on
 93 generation (Peltier & Clark 1979), and re-absorption of lee wave energy in a vertically
 94 sheared flow that decreases away from the topography (Kunze & Lien 2019). Nikurashin &
 95 Ferrari (2010b) performed idealised simulations representative of lee wave generation and
 96 dissipation in the Southern Ocean, finding that 50% of lee wave energy dissipated in the
 97 bottom 1km of the ocean for $Fr_L \geq 0.5$ compared to 10% for $Fr_L = 0.2$. A more realistic
 98 simulation capturing the characteristic stratification, wind forcing, and topography of the SO
 99 (Nikurashin *et al.* 2012) found that 80% of the wind power input into geostrophic eddies was
 100 converted to smaller scales by topography, of which just 20% radiated into the interior ocean,
 101 with most dissipated in the bottom 100 m. However, this and other wave resolving models
 102 may use artificially high diffusivity and viscosity, preventing lee waves from radiating in a
 103 physical way (Shakespeare & Hogg 2017).

104 The linear theory of Bell (1975) uses a freely radiating upper boundary condition (hereafter
 105 referred to as ‘unbounded’ theory), and can only be applied for uniform stratification
 106 and velocity, or by using the Wentzel-Kramers-Brillouin (WKB) approximation in some
 107 cases (Gill 1982; de Marez *et al.* 2020). This has led most idealized oceanic lee wave
 108 studies to assume the same and treat lee waves as a process confined to the deep ocean
 109 where stratification and velocity are assumed to be approximately constant with height. The
 110 assumption in most such studies (with some exceptions, e.g. Zheng & Nikurashin (2019)) is
 111 that no significant amount of lee wave energy reaches the surface, and even if it does, it does
 112 not matter for the structure of the wave field. In this study, we consider the treatment of lee
 113 waves as a full water column process, allowing reflection from the surface and interaction
 114 with changes in stratification and velocity with height.

115 In the real, dissipative ocean, some lee wave energy will be lost immediately due to
 116 boundary processes, and on their passage through the water column lee waves can be expected
 117 to lose energy through nonlinear processes leading to cascade of energy to smaller and
 118 eventually dissipative scales. Any model that tries to capture the entire water column must
 119 therefore include some representation of mixing and dissipation. However, the question of
 120 the magnitude and location of lee wave energy loss is a circular one, since it is the nonlinear
 121 interactions involving the wave field itself that cause wave breaking, leading to mixing and
 122 dissipation. Parametrisations for energy loss must therefore be used even when the lee waves
 123 are resolved, since capturing the lengthscales of both lee waves ($\sim O(5 \text{ km})$) and turbulent
 124 lengthscales ($\sim O(1 \text{ cm})$) in a 3D direct numerical simulation (DNS) remains prohibitively
 125 expensive. Shakespeare & Hogg (2017) investigated the impact of Laplacian parametrisation
 126 of mixing and dissipation in lee wave resolving models, and concluded that care must be
 127 taken to avoid artificially high viscosity and diffusivity that is not physically justified. They
 128 suggest that high levels of dissipation near the bottom boundary in wave resolving models
 129 could be a direct result of the high levels of viscosity and diffusivity used in the sub-gridscale
 130 parametrisation. Therefore, lee wave dissipation in the abyssal ocean could be commonly
 131 overestimated in modelling studies, preventing the radiation of lee wave energy far up into
 132 the water column.

133 Observations of lee waves are sparse due to their unpredictable generation by the time
 134 varying eddy field, difficulty in taking measurements at the bottom of the ocean, and their

135 steady nature (Legg 2021). However, the available observational evidence indicates that
136 linear predictions of energy flux exceed the levels of dissipation in the bottom 1 km by up
137 to an order of magnitude (Brearley *et al.* 2013; Sheen *et al.* 2013; Waterman *et al.* 2013).
138 Direct measurements of lee wave energy flux over the Shackleton fracture zone in the Drake
139 Passage (Cusack *et al.* 2017) were found to be consistent with predicted linear generation
140 modified for finite amplitude topography, but dissipation integrated over the water column
141 was found to be two orders of magnitude smaller than expected, suggesting that lee waves
142 find a sink for their energy outside of local mixing and dissipation.

143 One possible sink is reabsorption of lee wave energy to a sheared mean flow when the flow
144 is decreasing in magnitude away from topography (Kunze & Lien 2019). This is particularly
145 relevant in regions of enhanced bottom velocities, and is supported by observational evidence
146 that locations of overpredicted lee wave dissipation rates in the ACC are characterised by
147 large near-bottom velocities (Waterman *et al.* 2014). Observations taken from moorings in
148 the Scotia Sea also show evidence of interaction between internal waves and eddies, with
149 leading order impact on both wave and eddy energy budgets (Cusack *et al.* 2020). Zheng &
150 Nikurashin (2019) investigated another possible pathway, showing that lee wave energy
151 can be swept downstream to dissipate elsewhere. An important component to their study is
152 an upper boundary, which allows lee waves at scales affected by rotation or nonhydrostatic
153 effects to travel downstream by first reflecting at the upper boundary. They find that wave
154 reflection enhances energy dissipation rates in the interior by up to a factor of two.

155 The motivation for the current study arises from realistic regional simulations of the
156 Southern Ocean that show large lee waves penetrating high into the water column and
157 reflecting from the surface. Figure 1 shows vertical velocities from a recent nested simulation
158 of the Drake Passage at 0.01° resolution, performed using the hydrostatic configuration of
159 the Massachusetts Institute of Technology general circulation model (MITgcm, Marshall
160 *et al.* 1997). For details of the model setup see Mashayek *et al.* (2017) - the model shown
161 here has an improvement of vertical resolution from 100 to 225 vertical levels, with 10 m
162 resolution at the surface and ≤ 25 m for all depths above -4500 m, allowing better resolution
163 of the energetic internal wave field. The vertical diffusivity and viscosity have background
164 values of $5 \times 10^{-5} \text{ m}^2 \text{ s}^{-1}$, and are enhanced by the K -profile parametrisation with the critical
165 Richardson number for shear instability set to $Ri_c = 0.3$ (Large *et al.* 1994). Biharmonic Leith
166 horizontal viscosity is used with a coefficient of 2 (Leith 1996; Fox-Kemper & Menemenlis
167 2008).

168 Figure 1a shows a plan view of a typical daily average of vertical velocity at 200 m depth.
169 Lee waves appear as disturbances in the vertical velocity with $O(0.1^\circ) \sim O(6 \text{ km})$ horizontal
170 wavelength. Figure 1b shows the corresponding vertical velocity on a slice, with strong lee
171 wave generation at the very rough bottom topography and propagation throughout the water
172 column. The vertical velocities are near zero at the surface, with vertical phase lines and a
173 modal structure in the vertical indicative of superposition of the wave field due to reflection
174 at the surface.

175 This phenomenon has also been seen in other realistic simulations. de Marez *et al.* (2020)
176 examined the interaction of the Gulf Stream with the Charleston Bump in high resolution
177 realistic simulations, with a focus on lee wave generation. They found that the lee waves
178 have a surface signature, and showed qualitative agreement with sun glitter images from
179 satellite observations. The simulation output was compared with (unbounded) linear theory,
180 and differences noted near the surface, where surface reflection in the simulations caused a
181 modal structure in the vertical velocity.

182 Rosso *et al.* (2015) investigated topographic influence on surface submesoscales using a
183 realistic $1/80^\circ$ resolution model of the Indian sector of the Southern Ocean, and noted surface
184 peaks in vertical velocity (their figure 3). Lee waves reaching the surface were identified in

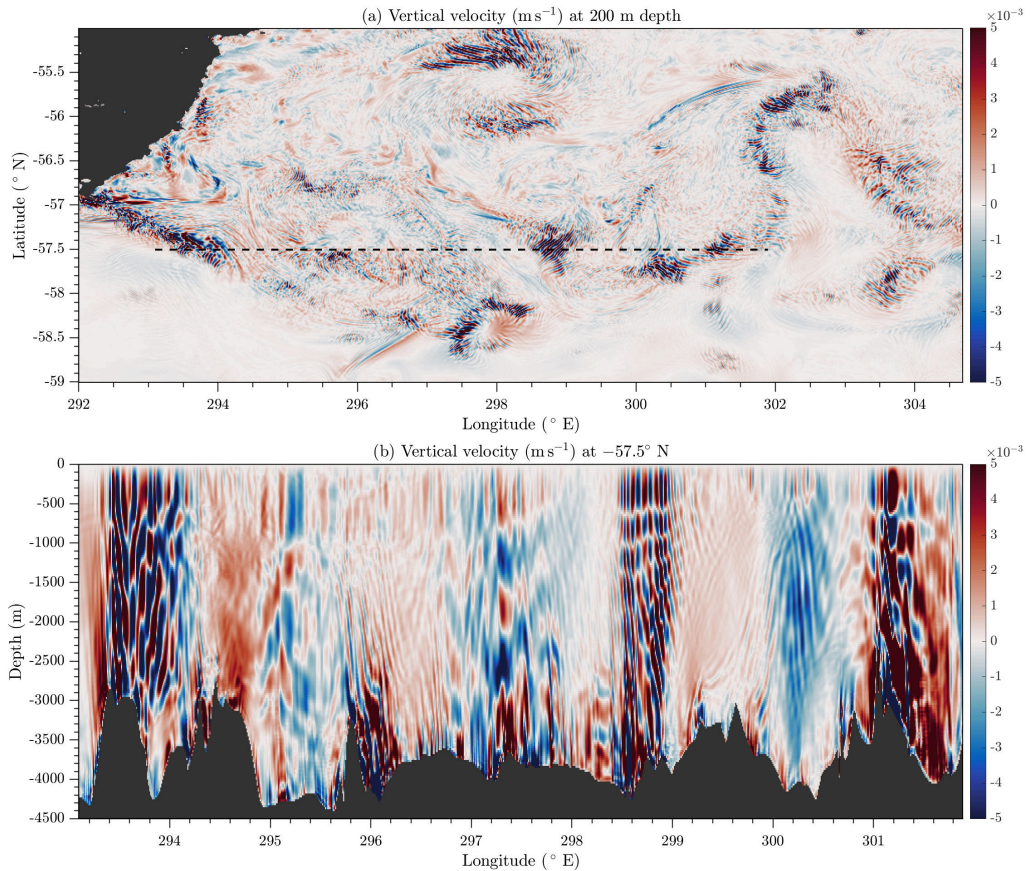


Figure 1: A daily average of vertical velocity (m s^{-1}) in a realistic simulation of the Drake Passage showing a strong lee wave field throughout the water column (details in main text). (a) A plan view at 200 m, and (b) a vertical slice through the dashed line in (a).

185 the simulations and noted as a potential source for these increased vertical velocities, but not
 186 investigated further as the focus was on vertical velocities caused by surface submesoscales.
 187 They reasoned that enhanced near surface vertical velocities in their figure 4d are unlikely to
 188 be generated by a lee wave evident at depth, both because the near surface vertical velocities
 189 have a vertical phase line, indicating that it is decoupled from the tilted lee wave phase lines
 190 below, and the RMS vertical velocity has a near surface maximum. However, we will show
 191 that vertical phase lines near the surface and a subsurface maximum in RMS vertical velocity
 192 are expected properties of lee waves that interact with the surface.

193 Bachman *et al.* (2017) simulated a similar region of the Drake Passage to that shown
 194 in figure 1a to investigate the surface submesoscale field and vertical velocities. They
 195 found regions of surface intensified RMS vertical velocity, and suggested that submesoscale
 196 circulations may not account for all such vertical velocities, with lee waves a potential source.
 197 In any case, the separation of surface submesoscales and lee waves is not clear due to their
 198 similar horizontal scales, and it is possible that they interact as a result.

199 Although there is evidence for near-surface lee wave structures in the above modelling
 200 studies, observational evidence is more scarce. In the Gulf Stream, synthetic aperture radar
 201 (SAR) and sun glitter images from satellites have been used to diagnose the presence of lee
 202 waves downstream of seamounts (Zheng *et al.* 2012; de Marez *et al.* 2020), and strongly

203 suggest interaction between bottom generated internal waves and the surface. In one of the
 204 few in-situ observations of lee waves, Cusack *et al.* (2017) found evidence of enhanced
 205 vertical velocities throughout the water column all the way to the top 500 m of the ocean
 206 above a ridge of 2500 m depth in the Drake Passage, suggesting interaction between the large
 207 wave generated at the ridge and the surface. However, the authors aren't aware of any direct
 208 observational evidence in the Southern Ocean for interaction between the bottom generated
 209 internal wave field and the surface.

210 A rigid lid upper boundary condition for the lee wave problem has been considered in the
 211 past, and the resonant properties of the solutions investigated (Bretherton 1969; McIntyre
 212 1972; Baines 1995). Dossmann *et al.* (2020) recently performed experiments to quantify the
 213 generation of topographic waves from a background flow with both steady and oscillatory
 214 components, developing a corresponding linear theory including both a rigid lid upper
 215 boundary and a Rayleigh friction to allow weakly viscous effects. Although coupling of
 216 the wave generation from quasi-steady flows and tides is the focus of their study, the linear
 217 theory is similar to our study of the steady component. Here, we also consider non-uniform
 218 background flows.

219 The radiation of lee waves under a changing background flow has been extensively studied
 220 in the atmospheric context, with a focus on parametrising wave drag due to isolated obstacles
 221 (mountains) in atmospheric models (Teixeira 2014, and references therein). Particularly
 222 relevant are studies of trapped lee waves, whereby sharp changes in background flow with
 223 height allow partial wave reflection and resonance (Scorer 1949; Gill 1982; Teixeira *et al.*
 224 2005, 2013), leading to high and low drag states, with clear parallels with the resonances
 225 found due to the upper boundary in the current study. In particular, Bretherton (1969)
 226 performed a comprehensive linear study including a rigid lid boundary condition similar to
 227 ours. However, a rigid lid condition in the atmosphere is not realistic, so efforts were generally
 228 made to improve the treatment of the upper boundary and reduce its impact (Teixeira 2014).
 229 This study is intended to demonstrate simple properties of oceanic lee waves under changing
 230 background conditions typical of the ocean, with a particular focus on their structure in the
 231 upper ocean due to the boundary condition at the surface. Typically, atmospheric lee wave
 232 studies focus on drag. In the oceanic context, both lee wave drag and mixing are important,
 233 thus our focus is also somewhat different to the aforementioned atmospheric studies.

234 The structure of this paper is as follows. In §2, we review and derive the linear lee wave
 235 theory with viscous and diffusive terms and discuss boundary conditions, energetics, time
 236 dependence, WKB solutions, and complications associated with the bounded solution and
 237 non-uniform background fields including resonance and critical levels. In §3, we present the
 238 numerical solver in a bounded and unbounded domain and describe the modelling set-up.
 239 We present results from the linear solver in §4, and discuss conclusions in §5.

240 2. Theoretical Framework

241 Following Bell (1975), we start from the rotating, incompressible, Boussinesq equations with
 242 the inclusion of Laplacian viscosity \mathcal{A} and diffusivity \mathcal{D} :

$$243 \quad \mathbf{u}_t^\dagger + \mathbf{u}^\dagger \cdot \nabla \mathbf{u}^\dagger + \mathbf{f} \times \mathbf{u}^\dagger = -\rho_0^{-1} \nabla p^\dagger + b^\dagger \hat{\mathbf{z}} + \mathcal{A} \nabla^2 \mathbf{u}^\dagger, \quad (2.1)$$

$$244 \quad b_t^\dagger + \mathbf{u}^\dagger \cdot \nabla b^\dagger = \mathcal{D} \nabla^2 b^\dagger, \quad (2.2)$$

$$245 \quad \nabla \cdot \mathbf{u}^\dagger = 0, \quad (2.3)$$

247 where $\mathbf{u}^\dagger = (u^\dagger, v^\dagger, w^\dagger)$ is the velocity, $\mathbf{f} = (0, 0, f)$ is the Coriolis parameter, p^\dagger is the
 248 pressure (with the linear hydrostatic pressure $-\rho_0 g(z - H)$ due to the constant reference

249 density ρ_0 removed), $b^\dagger = -(\rho^\dagger - \rho_0)g/\rho_0$ is the buoyancy, ρ^\dagger is the density, and \dagger is used
 250 to denote total (background plus wave) fields.

251 2.1. Base state

252 We specify that the background velocity is in the x -direction, and both background velocity
 253 and stratification are steady and vary only in the vertical. The background velocity is given
 254 by $(U(z), 0, 0)$, pressure by $\bar{p}(y, z)$, and buoyancy by $\bar{b}(y, z)$, with the bar notation indicating a
 255 background field. Assuming that the impact of perturbations on the mean flow is not leading
 256 order, from (2.1) it must satisfy both geostrophic and hydrostatic balance:

$$257 \quad -fU = -\rho_0^{-1}\bar{p}_y, \quad (2.4)$$

$$258 \quad 0 = -\rho_0^{-1}\bar{p}_z + \bar{b}. \quad (2.5)$$

260 Eliminating \bar{p} from (2.4) - (2.5) gives the thermal wind balance:

$$261 \quad -fU_z = \bar{b}_y. \quad (2.6)$$

262 Requiring that the stratification $N^2 = \bar{b}_z$ is a function of z only, (2.6) gives that $fU_{zz} = 0$.
 263 We therefore only consider base states such that $fU_{zz} = 0$, but continue the derivation for
 264 general $U(z)$ for use when $f = 0$. This ensures that although \bar{p} and \bar{b} are functions of y ,
 265 \bar{p}_y and \bar{b}_y are not, and the problem remains effectively 2D so that all coefficients of the
 266 linearised problem to be derived in §2.3 are independent of y .

267 2.2. Energy loss

268 A representation of lee wave energy loss is crucial to understanding the structure of the lee
 269 wave field in the vertical. Lee wave energy must either be reabsorbed by the mean flow,
 270 or lost to dissipation and mixing. The latter is a result of energy transfer to smaller scales
 271 through instabilities of the waves themselves, or through nonlinear interactions with other
 272 waves and the background flow. In our idealised linear model, we cannot properly represent
 273 either the dynamics of the waves which can lead to instabilities and breaking, or small scales
 274 from other sources of turbulence that act to eventually dissipate even linear waves. The effect
 275 of this energy lost from the lee wave field must therefore be parametrised.

276 Parametrisation of dissipation and mixing at the sub-gridscale in models is generally im-
 277 plemented through Laplacian (or higher order) viscous and diffusive terms in the momentum
 278 and buoyancy equations - as shown in (2.1) - (2.2). Shakespeare & Hogg (2017) provide a
 279 comprehensive overview of the role of Laplacian viscosity and diffusivity in the linear lee
 280 wave problem, with a focus on preventing excessive dissipation in wave resolving models.
 281 Here, we do not represent the processes that drain energy from the lee wave field, so aim
 282 to model them diffusively with this parametrisation. However, unlike Shakespeare & Hogg
 283 (2017), we are dealing with background flows that vary in the vertical, and thus including
 284 the vertical components $\mathcal{A}_v \mathbf{u}_{zz}^\dagger$ and $\mathcal{D}_v b_{zz}^\dagger$ of the Laplacian terms in our study significantly
 285 complicates the solution.

286 For mathematical convenience, we therefore represent the total viscous and diffusive
 287 terms by the horizontal components only. This allows some scale selection for energy loss
 288 (improving on, say, a simple Rayleigh friction), without overly complicating the problem.
 289 Using only the horizontal component as a proxy for the total dissipation and mixing
 290 has certain drawbacks, including invalidating any solutions where the vertical wavelength
 291 changes drastically or becomes very small, e.g. at critical levels. It is important to keep in
 292 mind the simplifications made here when analysing the model mixing and dissipation in

293 §4. Direct comparisons between our horizontal turbulent viscosity \mathcal{A}_h and diffusivity \mathcal{D}_h
 294 parameters and other studies or models should also be made with care, since they represent
 295 both horizontal and vertical viscosity and diffusivity. Furthermore, since \mathcal{A}_h and \mathcal{D}_h represent
 296 both background turbulent processes and breaking of the lee wave field itself, their ‘real’
 297 values should depend on nonlinearity of the wave field and properties of the background
 298 flow, among other things. Although the simplifications made with this parametrisation are
 299 likely to modify our solutions somewhat, we believe that the key results of this study are
 300 unaffected.

301 2.3. Linearisation

302 For $Fr_L \ll 1$, we consider small perturbations to the base state described in §2.1. We consider
 303 a quasi-2D flow such that the topography and waves are uniform in y . This choice is sufficient
 304 to demonstrate our main findings and greatly simplifies the problem, although the theory
 305 can be extended to 2D topography without significant difficulties. The coefficients of the
 306 linearised equations are independent of y due to the constraints on the base state described
 307 in §2.1, thus the perturbation variables can be taken to be independent of y . We also assume
 308 here that the perturbations are steady, although this need not be imposed at this point and
 309 follows from the application of the steady boundary conditions to be described in §2.4.

310 Letting $\mathbf{u}^\dagger = (U(z) + u(x, z), v(x, z), w(x, z))$, $b^\dagger = \bar{b}(y, z) + b(x, z)$, $p^\dagger = \bar{p}(y, z) + p(x, z)$
 311 and linearising (2.1) - (2.3) gives:

$$312 \quad wU_z + Uu_x - fv = -\rho_0^{-1}p_x + \mathcal{A}_h u_{xx}, \quad (2.7)$$

$$313 \quad Uv_x + fu = \mathcal{A}_h v_{xx}, \quad (2.8)$$

$$314 \quad \alpha U w_x = -\rho_0^{-1}p_z + b + \alpha \mathcal{A}_h w_{xx}, \quad (2.9)$$

$$315 \quad Ub_x - fvU_z + wN^2 = \mathcal{D}_h b_{xx}, \quad (2.10)$$

$$316 \quad u_x + w_z = 0, \quad (2.11)$$

318 where $\alpha \in \{0, 1\}$, so that when $\alpha = 0$ the equations are hydrostatic. The hydrostatic
 319 assumption is made when the ratio of vertical to horizontal scales is small, as is often
 320 the case for lee waves. We introduce a perturbation streamfunction ψ such that $u = -\psi_z$,
 321 $w = \psi_x$, with Fourier transform $\hat{\psi}(k, z)$ defined such that:

$$322 \quad \psi(x, z) = \frac{1}{2\pi} \int_{-\infty}^{\infty} \hat{\psi}(k, z) e^{ikx} dk. \quad (2.12)$$

323 Taking the Fourier transform in x of (2.7) - (2.11) and solving for the transformed
 324 streamfunction $\hat{\psi}(k, z)$ gives a second order ordinary differential equation:

$$325 \quad \hat{\psi}_{zz} + P(k, z)\hat{\psi}_z + Q(k, z)\hat{\psi} = 0, \quad (2.13)$$

326 where

$$327 \quad P(k, z) = \frac{f^2 U_z (2U - ik(\mathcal{A}_h + \mathcal{D}_h))}{(k^2(U - ik\mathcal{A}_h)^2 - f^2)(U - ik\mathcal{A}_h)(U - ik\mathcal{D}_h)}, \quad (2.14)$$

$$328 \quad Q(k, z) = \frac{k^2(U - ik\mathcal{A}_h)(N^2 - \alpha k^2(U - ik\mathcal{A}_h)(U - ik\mathcal{D}_h))}{(U - ik\mathcal{D}_h)(k^2(U - ik\mathcal{A}_h)^2 - f^2)} - \frac{k^2 U_{zz}(U - ik\mathcal{A}_h)}{k^2(U - ik\mathcal{A}_h)^2 - f^2}. \quad (2.15)$$

330 With constant background velocity and stratification and in the absence of viscosity and

331 diffusivity, this reduces to the familiar equation for the steady lee wave problem (Bell 1975):

$$332 \quad \hat{\psi}_{zz}(k, z) + k^2 \frac{N^2 - \alpha U^2 k^2}{U^2 k^2 - f^2} \hat{\psi}(k, z) = 0, \quad (2.16)$$

333 with solution:

$$334 \quad \hat{\psi}(k, z) = A(k)e^{im(k)z} + B(k)e^{-im(k)z}, \quad (2.17)$$

335 for some functions A and B to be specified by the boundary conditions, where

$$336 \quad m^2(k) = k^2 \frac{N^2 - \alpha U^2 k^2}{U^2 k^2 - f^2}. \quad (2.18)$$

337 It is clear from (2.17) and (2.18) that there are radiating solutions (lee waves) only when m
338 is real, that is when the topographic wavelength k satisfies

$$339 \quad |f| < |Uk| < |N|. \quad (2.19)$$

340 For wavenumbers k in this radiating range, rotation can be neglected when $|f| \ll |Uk|$, and
341 the hydrostatic assumption ($\alpha = 0$) can be made when $|Uk| \ll |N|$, since in this case the
342 vertical wavenumber $m \sim \frac{N}{U}$ (from (2.18)), so $|Uk|/|N|$ represents the ratio of vertical to
343 horizontal wavelengths.

344 2.4. Boundary conditions

345 2.4.1. Bottom boundary condition

346 For a given k , (2.13) requires two boundary conditions. A free slip condition to ensure that
347 the flow is parallel to the 2D topography $h(x)$ is given by:

$$348 \quad w^\dagger(x, h) = u^\dagger(x, h)h_x. \quad (2.20)$$

349 Linearising about the base state then gives:

$$350 \quad w(x, 0) = U(0)h_x, \quad (2.21)$$

351 or equivalently, defining the Fourier transform of the topography $\hat{h}(k)$ similarly to (2.12):

$$352 \quad \hat{\psi}(k, 0) = U(0)\hat{h}(k). \quad (2.22)$$

353 Given this requirement, we write $\hat{\psi}(k, z) = U(0)\hat{h}(k)\hat{\zeta}(k, z)$, where $\hat{\zeta}(k, z)$ is the normalised
354 vertical structure function for a wavenumber k , so that

$$355 \quad \psi(x, z) = \frac{U(0)}{2\pi} \int_{-\infty}^{\infty} \hat{\zeta}(k, z)\hat{h}(k)e^{ikx} dk, \quad (2.23)$$

356 and $\hat{\zeta}(k, z)$ satisfies

$$357 \quad \hat{\zeta}_{zz} + P(k, z)\hat{\zeta}_z + Q(k, z)\hat{\zeta} = 0, \quad (2.24)$$

$$358 \quad \hat{\zeta}(k, 0) = 1. \quad (2.25)$$

360 2.4.2. Upper boundary condition

361 For the second condition, first consider the classical unbounded lee wave problem, which
362 requires that waves propagate freely through the upper boundary. When the background flow
363 is uniform in z , P vanishes, Q is constant in z , and a vertical wavenumber $m(k) = \pm\sqrt{Q(k)}$
364 can be found. If the flow is also inviscid, $m(k)$ is given up to a sign by (2.18), and for the
365 wavelike solutions with k in the radiating range (2.19), there is then a well defined vertical
366 group velocity (to be discussed further in §2.5). The vertical group velocity must be positive

367 when the solutions are wavelike so that energy radiates away from topography, and this is
 368 ensured by choosing $m(k)$ to have the same sign as Uk . When m is imaginary (non-wavelike
 369 solutions), physical intuition necessitates that the positive root is taken so that disturbances
 370 decay away from topography rather than increase exponentially (see (2.17)).

371 If viscosity and diffusivity are non-zero, there is still a well defined complex vertical
 372 wavenumber $m(k) = \pm\sqrt{Q(k)}$. However, since m is now complex, the correct choice for
 373 the sign of m must always be that with positive imaginary part so that the solution decays
 374 away from the topography. Note that the previously non-radiating wavenumbers gain a small
 375 radiating component, although this is insignificant in the realistic limit of weak viscosity and
 376 diffusivity - see Shakespeare & Hogg (2017) for a detailed discussion. Here, we consider
 377 radiating lee waves from topography such that $|f| < |U(0)k| < |N(0)|$.

378 When the coefficients P and Q are not constant in z , this radiating upper boundary condition
 379 is in general poorly defined, since for each k there is not a well defined vertical wavelength
 380 and group velocity. Waves can internally reflect and refract from changes in background
 381 density or velocity, so the solution cannot be restricted to upward propagating components.
 382 However, in some cases WKB solutions can be found for slowly varying background flows -
 383 see §2.11.

384 If lee waves reach the upper ocean, the radiating upper boundary condition is inappropriate,
 385 and the air-sea interface may instead be better represented by a free surface boundary
 386 condition. A simpler condition is the rigid lid - we will show that for this problem, these are
 387 essentially equivalent.

388 At a free surface given by $z = H + \eta(x)$, where $\eta \ll H$, the linearised kinematic boundary
 389 condition (c.f. (2.21)) is:

$$390 \quad \psi(x, H) = U(H)\eta(x). \quad (2.26)$$

391 A further boundary condition is required to close the problem and is given by the dynamic
 392 condition that the pressure at the surface is equal to the atmospheric pressure p_A (assumed
 393 constant). The full pressure at the surface is $p^\dagger(x, z) = \bar{p}(z) + p(x, z)$, plus the linear term
 394 $-\rho_0g(z - H)$ that was removed in the definition of p^\dagger (see (2.1)). Expanding $p^\dagger(x, H + \eta(x))$
 395 to first order in the perturbation variables and η , and using $\bar{p}(H) = p_A$, gives:

$$396 \quad p^\dagger(x, H + \eta(x)) \simeq p^\dagger(x, H) + \eta(x) \left. \frac{\partial p^\dagger}{\partial z} \right|_{z=H}, \quad (2.27)$$

$$397 \quad \simeq p_A + p(x, H) + \eta(x) \left. \frac{\partial \bar{p}}{\partial z} \right|_{z=H}. \quad (2.28)$$

399 Invoking the boundary condition then gives:

$$400 \quad p_A = p_A + p(x, H) + \eta(x) \left. \frac{\partial \bar{p}}{\partial z} \right|_{z=H} - \rho_0g\eta(x) \quad (2.29)$$

401 Using hydrostatic balance of the base state (2.5) then gives the dynamic boundary condition:

$$402 \quad p(x, H) = \rho_0(g - \bar{b}(H))\eta(x) = \bar{\rho}(H)g\eta(x) = \rho_0g\eta(x), \quad (2.30)$$

403 where the reference density ρ_0 is taken to be the base state surface density.

404 Eliminating the unknown η from the surface boundary conditions (2.26) and (2.30) gives
 405 the boundary condition:

$$406 \quad \psi(x, H) = \frac{U(H)p(x, H)}{\rho_0g}. \quad (2.31)$$

407 This surface boundary condition could be used with the bottom boundary condition (2.21)
 408 to solve (2.7) - (2.11), then the surface height recovered from (2.30) or (2.26). However, in

409 practise this is unnecessary, as (2.31) can be well approximated by the rigid lid condition
 410 $\psi(x, H) = 0$, equivalent to imposing $\eta(x) = 0$ (and thereby not satisfying the dynamic
 411 boundary condition). To see why, first notice from (2.7) that for negligible rotation, shear,
 412 and viscosity, $p \sim -\rho_0 U u \sim \rho_0 U \psi_z$. For slowly varying background conditions, we expect
 413 $\psi(x, z)$ to locally have a sinusoidal structure in the vertical, so let (for fixed x):

$$414 \quad \psi(z) \sim A \sin(mz + \theta), \quad (2.32)$$

$$415 \quad \psi_z(z) \sim Am \cos(mz + \theta), \quad (2.33)$$

417 for some amplitude A , wavenumber m , and phase θ . Then, using the boundary relation (2.31):

$$418 \quad \sin(mH + \theta) \sim \frac{mU^2}{g} \cos(mH + \theta). \quad (2.34)$$

419 Assuming that $m \sim N/U$ (the hydrostatic, non-rotating limit of (2.18)):

$$420 \quad \tan(mH + \theta) \sim \frac{NU}{g} \ll 1, \quad (2.35)$$

421 even for large upper ocean values of U and N , and this scaling still holds for realistic conditions
 422 with rotation and nonhydrostatic waves. Therefore, the phase θ is such that $\psi(H) \simeq 0$, and
 423 it is clear that a rigid lid approximation is sufficient for determining the interior structure of
 424 the lee waves. The full free surface boundary condition could be implemented to determine
 425 exactly the (linear) surface height $\eta(x)$, but hereafter we only consider the rigid lid boundary
 426 condition. Since the interior flow is relatively unaffected by this approximation, we could
 427 still estimate the surface height without explicitly solving for it, using (2.30):

$$428 \quad \eta(x) \sim \frac{p(x, H)}{\rho_0 g}, \quad (2.36)$$

429 where $p(x, H)$ is found from the rigid lid solution.

430 With the rigid lid condition $\psi(x, H) = 0$, the solution to the bounded problem is then given
 431 by (2.24) - (2.25), with the upper boundary condition:

$$432 \quad \hat{\zeta}(k, H) = 0. \quad (2.37)$$

433 2.5. Group velocities

434 The behaviour of lee waves in a bounded domain depends strongly on the direction of their
 435 group velocity. Consider the inviscid and unbounded problem with uniform background
 436 stratification and velocity, so that the vertical wavenumber m is independent of z . Re-deriving
 437 the governing equation (2.16) with time dependence by considering plane wave solutions
 438 $\sim e^{i(kx+mz-\omega t)}$ gives the dispersion relation (c.f. (2.18)):

$$439 \quad (\omega - Uk)^2 = \frac{N^2 k^2 + f^2 m^2}{\alpha k^2 + m^2}, \quad (2.38)$$

440 where $\omega = 0$ for steady lee waves satisfying the boundary condition (2.21). The phase velocity
 441 is zero as a result, but the group velocity is non zero and can be found by differentiating
 442 (2.38):

$$443 \quad \mathbf{c}_g = \left(\frac{\partial \omega}{\partial k}, \frac{\partial \omega}{\partial m} \right), \quad (2.39)$$

$$444 \quad = \left(\frac{f^2(N^2 - \alpha U^2 k^2) + \alpha U^2 k^2(U^2 k^2 - f^2)}{Uk^2(N^2 - \alpha f^2)}, \frac{(U^2 k^2 - f^2)^{\frac{3}{2}}(N^2 - \alpha U^2 k^2)^{\frac{1}{2}}}{Uk^2(N^2 - \alpha f^2)} \right), \quad (2.40)$$

445

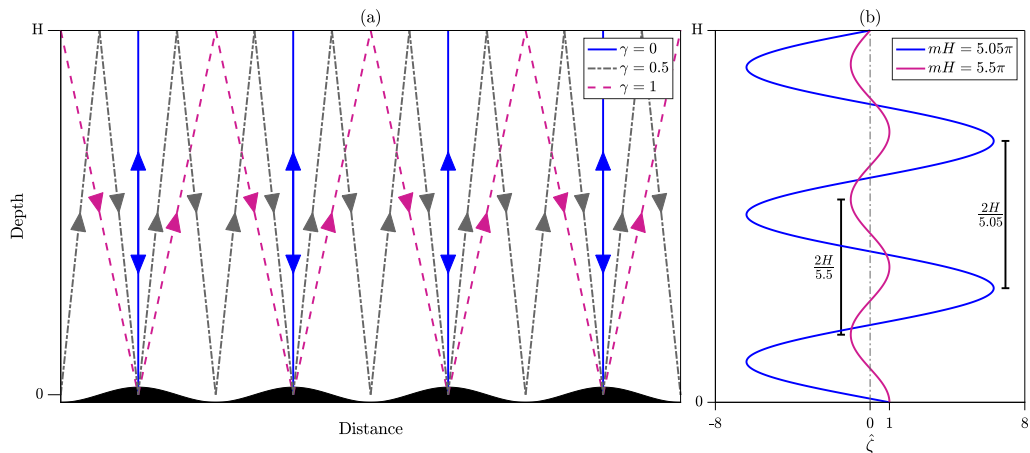


Figure 2: a) Diagram showing monochromatic topography with indicative ray paths for several values of the overlap parameter γ , demonstrating some possible idealised paths of lee waves with different directions of group velocity. b) Diagram showing the vertical structure function $\hat{\zeta}(k, z)$ for the analytic solution (2.42), for some vertical wavenumbers m such that the solution is near-resonant (blue) and at its minimum amplitude (magenta).

446 where the sign of the vertical group velocity is taken to be positive when m is real, as is
 447 appropriate for the unbounded case, and it is assumed that $|f| < |Uk| < |N|$ so that the waves
 448 are radiating. It is clear from (2.40) that in the non-rotating and hydrostatic case ($f = \alpha = 0$),
 449 the horizontal component of group velocity is zero, and waves propagate vertically upwards.
 450 Supposing now that they encounter the surface, the waves will reflect and propagate directly
 451 downwards - still with zero horizontal group velocity and now with negative vertical group
 452 velocity - superimposing exactly on the upward propagating wave field. This scenario is
 453 illustrated for monochromatic topography in figure 2a (blue lines). The reflected waves can
 454 then be expected to directly increase or decrease the topographic wave drag and energy
 455 conversion by constructive or destructive interference with the upwards propagating wave
 456 field at the topography. The extent to which this occurs is determined by the energy lost to
 457 mixing and dissipation during propagation, to be discussed in §4.1. When the horizontal
 458 group velocity is zero, no energy propagates downstream, so without dissipative energy loss
 459 there can be no energy conversion into lee waves at the topography and also no wave drag
 460 (see §2.8). However, there may be resonance (to be discussed in §2.7).

461 If $|Uk|$ is of comparable magnitude to the Coriolis or buoyancy frequency, the waves will
 462 have a positive horizontal component of group velocity and will propagate both upwards
 463 and downstream, reflecting at the surface downstream of the topography. Without dissipation
 464 and mixing this could continue indefinitely and allow the lee wave energy to propagate far
 465 downstream, although in reality it seems unlikely that a significant amount of wave energy
 466 would undergo multiple reflections due to nonlinear interactions near the bottom boundary.
 467 For flow moving over the top $\sim U/N$ of an isolated topographic peak and generating a
 468 continuous range of wavenumbers k , if the angle of propagation (the angle of the group
 469 velocity vector to the vertical) is large enough for all radiating components, the reflected
 470 wave will not significantly interact with the generation process and the wave drag will be
 471 unchanged from the unbounded case. If the bump is not isolated, the reflected wave could be
 472 incident on the generation of a lee wave at a different topographic feature, and the drag (and
 473 energy flux) modification would be more complex.

474 To determine the likelihood of a lee wave superimposing on itself at the topography, we
 475 can determine the angle of propagation using (2.40), assuming for simplicity that U and N

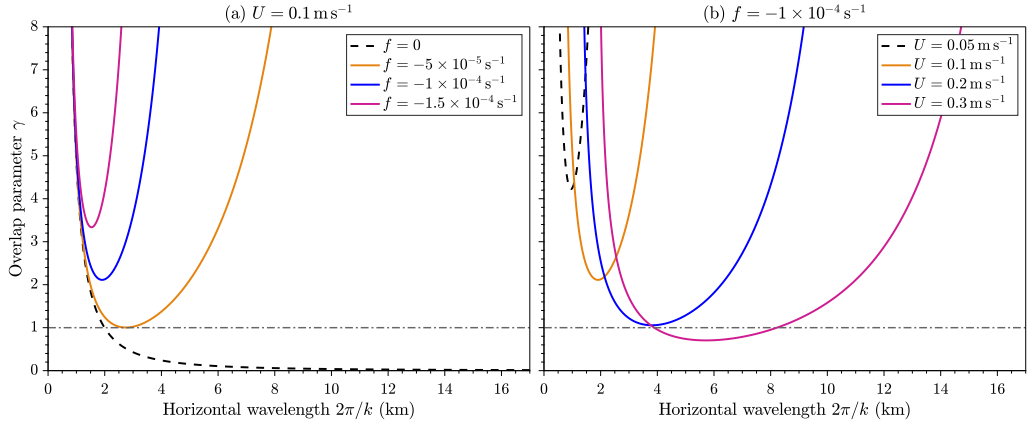


Figure 3: Overlap parameter γ defined in (2.41) for the nonhydrostatic case and (a) fixed $U = 0.1 \text{ m s}^{-1}$, varying f and (b) fixed $f = -1 \times 10^{-4} \text{ s}^{-1}$, varying U , with $H = 3 \text{ km}$, $N = 1 \times 10^{-3} \text{ s}^{-1}$. The black dashed line shows $\gamma = 1$, below which a reflected lee wave could be expected to modify its own generation mechanism.

476 are constant and viscosity and diffusivity are negligible. An ‘overlap parameter’ $\gamma(k)$ can be
 477 defined as:

$$478 \quad \gamma(k) = \left| \frac{kH}{\pi} \right| \tan \theta, \quad \tan \theta = \frac{\partial \omega}{\partial k} \bigg/ \frac{\partial \omega}{\partial m}, \quad (2.41)$$

479 where θ is the angle of wave propagation to the vertical, and for each k , γ is the horizontal
 480 distance travelled by a wave whilst propagating to the surface at $z = H$ and back to the
 481 topography at $z = 0$, normalised by the horizontal wavelength. This is illustrated for $\gamma =$
 482 0, 0.5, and 1 in figure 2a. Figure 3 shows the variation in γ with horizontal wavelength $2\pi/k$
 483 for various U and f . Each curve tends to infinity (not shown) at $k = |N/U|$ and $k = |f/U|$,
 484 at which point the vertical group velocity reaches zero and the solutions become evanescent.
 485 The increase in γ for both large and small horizontal wavelengths is due to the increasing
 486 downstream component of group velocity.

487 For smaller values of f (black dashed and orange lines in figure 3a) and larger values of U
 488 (blue and magenta lines in figure 3b), there exists a range of scales at which $\gamma \lesssim 1$, indicating
 489 that reflected lee waves could impact on the generation mechanism by direct superposition.
 490 For $f = -1 \times 10^{-4} \text{ s}^{-1}$, characteristic of the Southern Ocean, there exist horizontal scales
 491 at which this may be the case for $U \gtrsim 0.2 \text{ m s}^{-1}$. However, for $f = -1 \times 10^{-4} \text{ s}^{-1}$ and
 492 $U = 0.1 \text{ m s}^{-1}$ (orange line in figure 3b), $\gamma > 2$ for all radiating wavelengths, and all reflected
 493 waves return to topography at least 4 km downstream of the generating topographic feature.
 494 Of course, this argument doesn’t cover the more likely scenario of varying velocity and
 495 stratification with height. We conclude that for lee waves in shallow areas, low latitudes,
 496 or high background flows it is possible for lee waves generated by isolated topography to
 497 reflect at the surface and modify the original wave drag and energy conversion, but that this
 498 is unlikely for deep generation, low background velocities, and high latitudes.

499 When the topography is not isolated, and in particular when an artificially discrete
 500 topographic spectrum is used as in this study, the wave drag modification can be significant
 501 even when the overlap parameter is larger than one. For monochromatic topography, when
 502 $\gamma(k) = n \in \mathbb{N}$, a wave generated at a topographic peak reflects at the surface and is incident
 503 on the topographic peak n wavelengths downstream from the original, as shown in figure 2a
 504 for $n = 1$, and impacts the wave field at that generation site in a similar way to the case $\gamma = 0$.
 505

2.6. Analytic solution

When U and N are constant with height, so that P vanishes and Q is a function of k only, the solution to (2.24) for $\hat{\zeta}(k, z)$ is (extended from Baines (1995)):

$$\hat{\zeta}(k, z) = \frac{\sin(m(k)(H - z))}{\sin(m(k)H)}, \quad (2.42)$$

where $m(k)$ is the complex vertical wavenumber defined by $m^2(k) = Q(k)$, and the choice of sign does not matter. The solution can then be found numerically for general topography via (2.23), or analytically for monochromatic topography $h(x) = h_0 \cos k_0 x$ to be:

$$\psi(x, z) = U h_0 \Re \left(\frac{\sin(m(k_0)(H - z))}{\sin(m(k_0)H)} e^{i k_0 x} \right). \quad (2.43)$$

The above solutions are valid only when $|m(k)H| \neq n\pi$, $n \in \mathbb{N}$. At such points, resonances of the system occur.

2.7. Resonance

For uniform U and N , under the assumption that lee waves are hydrostatic ($|Uk| \ll |N|$), rotation is unimportant ($|Uk| \gg |f|$), and the system is inviscid, the vertical wavenumber is simply $m(k) = N/U$. The resonances of (2.42) are then independent of k , and occur when $|NH/U| = n\pi$ for some $n \in \mathbb{N}$. There are no steady solutions to (2.24), (2.25) and (2.37) in this inviscid limit. Physically, this occurs when a whole number of half-wavelengths fits in the vertical domain and there is constructive interference of the upwards and downwards propagating waves. Figure 2b shows the vertical structure function $\hat{\zeta}$, defined in (2.42), for two real values of m . When $mH = 5.05\pi$ (blue) the system is near resonance, as the half-wavelength nearly divides the depth H (true resonance is at $mH = 5\pi$). Thus, $\hat{\zeta}(z) = 0$ near $z = 0$, so in order to satisfy the boundary condition $\hat{\zeta}(z = 0) = 1$, the amplitude of the wave must be very large. At true resonance, this boundary condition cannot be met. In the opposite case, (shown for $mH = 5.5\pi$ in magenta), there is destructive interference and the amplitude is at a minimum.

Under the above assumptions, the horizontal group velocity is zero, therefore energy cannot escape downstream and the wave generation at resonance continually reinforces the wave field. If this were to happen in practise, the wave amplitude would become large enough to invalidate the linearity of the wave field, perhaps causing nonlinear wave breaking or modifying the wave field or the boundary condition so as to move the system away from resonance.

When nonhydrostaticity is included, the horizontal group velocity is non-zero and the nature of the resonance changes slightly. The vertical wavenumber $m(k) = \sqrt{N^2/U^2 - k^2}$, thus the solution (2.42) has singularities at

$$k^2 = \frac{N^2}{U^2} - \frac{n^2 \pi^2}{H^2}, \quad n \in \mathbb{N}. \quad (2.44)$$

Physically, these singularities still represent modes where an exact number of half vertical wavelengths fit in the domain, but now this happens at different values of U , N and H for each component k of the wave field.

Mathematically, the resulting singularities of (2.42) are simple poles, so when the topographic spectrum $\hat{h}(k)$ is continuous (as for isolated topography), the integral (2.23) along the real line can be moved to a contour of integration in complex k space that avoids the poles. To ensure that there is no disturbance at upstream infinity, the contour must be taken below rather than above the poles (McIntyre 1972). The solution can then be expressed as the

548 Cauchy principle value of (2.23) plus half the residues of the simple poles, which represent
 549 the nonhydrostatic resonant modes (Baines 1995). The solutions, when $\hat{h}(k)$ is continuous,
 550 could be found numerically from (2.23) by choosing some contour of integration sufficiently
 551 far from the poles to avoid numerical difficulties. However, this becomes more difficult once
 552 rotation is included since the poles no longer all lie on the real axis. The numerical solution
 553 is also problematic since periodicity in the horizontal is assumed by default when taking a
 554 discretised Fourier transform, leading to spurious waves upstream of the isolated topography.
 555 If the topographic spectrum is discrete and includes one of the singular wavelengths defined
 556 by (2.44), then true resonance occurs and no steady solution exists.

557 The inclusion of energy loss through viscosity and diffusivity aids the numerical solution
 558 by moving all poles off of the real line so that the integral (2.23) can be found numerically
 559 with a simple fast Fourier transform (FFT). Although true resonance is avoided, states can
 560 still be near resonant, as will be shown in §4.1. The topographic representation used here
 561 (see §3.3) consists of a spectrum of topographic wavenumbers, which numerically becomes
 562 a sum of discrete components. This is likely to enhance the resonance effect compared to a
 563 more realistic and inhomogeneous topography.

564 2.8. Energy and momentum

565 The vertical linear lee wave energy flux at a given height is given by \overline{pw} , where an overbar
 566 here represents a horizontal average. At the topography ($z = 0$), this is equal to the product
 567 of the bottom mean flow velocity and the horizontally averaged form drag exerted by the
 568 topography on the mean flow, since using (2.21):

$$569 \quad \overline{pw}|_{z=0} = U(0)\overline{ph_x}|_{z=0}. \quad (2.45)$$

570 Taking the inner product of (2.7) - (2.9) with the perturbation velocity and multiplying (2.10)
 571 by the perturbation buoyancy gives the energy equation for the wave field. Taking a horizontal
 572 average and assuming a periodic domain in the horizontal then gives an expression for the
 573 divergence of the energy flux:

$$574 \quad \overline{pw}_z = -\rho_0(U_z F + \overline{D}), \quad (2.46)$$

575 where $\overline{D} = \overline{\varepsilon} + \overline{\Phi}$ is the horizontally averaged energy loss from the flow, consisting of the
 576 dissipation rate $\varepsilon = \mathcal{A}_h |\mathbf{u}_x|^2$ and irreversible mixing $\Phi = \mathcal{D}_h b_x^2 / N^2$, and

$$577 \quad F = \overline{uw} - \frac{\overline{fvb}}{N^2} \quad (2.47)$$

578 is the wave pseudomomentum flux, or the Eliassen-Palm (E-P) flux (Eliassen & Palm 1960).
 579 If there are no critical levels ($U \neq 0$) it can be shown from (2.7) - (2.10) that the E-P flux F
 580 is related to the energy flux as (extended from Eliassen & Palm 1960):

$$581 \quad \overline{pw} = -\rho_0 U \left[\overline{(u - u_x \mathcal{A}_h / U) w} - \frac{f}{N^2} \overline{(b - \mathcal{D}_h b_x / U) v} \right] \quad (2.48)$$

$$582 \quad = -\rho_0 U F (1 + \mathcal{O}(\mathcal{A}_h k / U)), \quad (2.49)$$

584 where k is the characteristic wavenumber of the topography, and $\mathcal{A}_h \sim \mathcal{D}_h$. Taking typical
 585 values considered here, $\mathcal{A}_h \sim 1 \text{ m}^2 \text{ s}^{-1}$, $k \sim 0.005 \text{ m}^{-1}$, and $U \sim 0.1 \text{ m s}^{-1}$, giving $\mathcal{A}_h k / U \sim$
 586 $0.05 \ll 1$. Thus the energy flux is approximately equal to the local velocity multiplied by the
 587 E-P flux even when there is energy loss.

588 Since the source of the waves is at the bottom of the domain, the energy flux is always
 589 positive (or zero). (2.49) then gives that the E-P flux must have the opposite sign to U , thus
 590 $F \leq 0$ in the cases considered here. This can be seen from the form of F (2.47) in the

591 non-rotating case, since a positive vertical velocity perturbation of the flow ($w > 0$) will
 592 correspond to the deceleration of a fluid parcel in the horizontal ($u < 0$), thus the momentum
 593 flux $\overline{uw} \leq 0$.

594 In the inviscid problem, (2.46) and (2.49) together give (Eliassen & Palm 1960):

$$595 \quad F_z = 0. \quad (2.50)$$

596 Therefore, the E-P flux is conserved when there is no energy lost to dissipation and mixing.
 597 When there is also no vertical shear of the mean flow ($U_z = 0$), (2.46) gives that the energy
 598 flux $\overline{p\overline{w}}$ is also conserved. When the mean velocity increases or decreases with height, the
 599 energy flux increases or decreases correspondingly, but the E-P flux is still conserved. Any
 600 divergence of the E-P flux thus corresponds to the force exerted on the flow by the waves as
 601 they dissipate (Andrews & McIntyre 1976). It is the divergence of F rather than the Reynolds
 602 stress (or momentum flux) \overline{uw} that gives the relevant lee wave forcing on the mean flow,
 603 since \overline{uw} is in general not conserved - a paradox explained by Bretherton (1969).

604 The total wave drag on the mean flow (defined here to be a positive quantity, though acting
 605 in the negative x direction) is therefore given by the integral of $\rho_0 F_z$ over the depth of the
 606 ocean. Since there cannot be any energy or momentum flux through the upper boundary,
 607 $\overline{p\overline{w}}|_{z=H} = F(H) = 0$, thus the wave drag is given by $-\rho_0 F(0)$. Comparison of (2.45) and
 608 (2.49) then shows that up to $O(\mathcal{A}_h k/U)$ the wave drag is equal to the form drag.

609 Since $\overline{p\overline{w}}|_{z=H} = F(H) = 0$, if energy loss \overline{D} is zero, $F = 0$ everywhere (from (2.50)) and
 610 $\overline{p\overline{w}} = 0$ everywhere (from (2.49)), thus there is no net topographic wave drag on the flow
 611 or energy conversion to lee waves in steady state. This is true for a periodic domain - in a
 612 non-periodic domain the waves would propagate infinitely far downstream, and boundary
 613 fluxes would become important in the equations (2.46) and (2.49). Energy loss is therefore a
 614 key component of the bounded study, as there can be no topographic wave drag without it.
 615 This is a realisation of the ‘non-acceleration theorem’, first discussed by Charney (1961). Of
 616 course, in the unbounded problem there must also be energy loss in order to have wave drag
 617 at the topography - but that energy loss can implicitly occur by allowing the lee waves to exit
 618 the given domain (such that $\overline{p\overline{w}}|_{z=H} > 0$) and dissipate ‘elsewhere’.

619 From (2.46), the wave energy flux can change both by exchange with a mean flow through
 620 the E-P flux (Kunze & Lien 2019), and by mixing and dissipation. Integrating (2.46) over
 621 the entire height of the domain gives:

$$622 \quad \overline{p\overline{w}}|_{z=0} - \overline{p\overline{w}}|_{z=H} = \rho_0 \int_0^H U_z F + D \, dz. \quad (2.51)$$

623 If there is an upper boundary and no background shear ($U_z = 0$), then $\overline{p\overline{w}}|_{z=H} = 0$, and
 624 topographic energy conversion and wave drag are directly proportional to the total mixing
 625 and dissipation in the water column.

626 *2.9. Time dependence*

627 When calculating lee wave fluxes, it is usually assumed that the background fields and lee
 628 waves are steady. In reality, the geostrophic flows that generate lee waves vary on timescales
 629 of days to weeks. After a change in the background flow, the time taken for the lee wave field
 630 to equilibrate to the new steady state could be long compared to the typical timescales of the
 631 flow.

632 The relevant timescale in this study is the time taken for the lee wave to propagate from
 633 the topography to the surface. Figure 4 shows the vertical group velocity (defined in (2.40))
 634 for various values of f and U . Lee waves generated at smaller horizontal scales (larger
 635 k) propagate faster, although they are also more likely to dissipate along the way due to

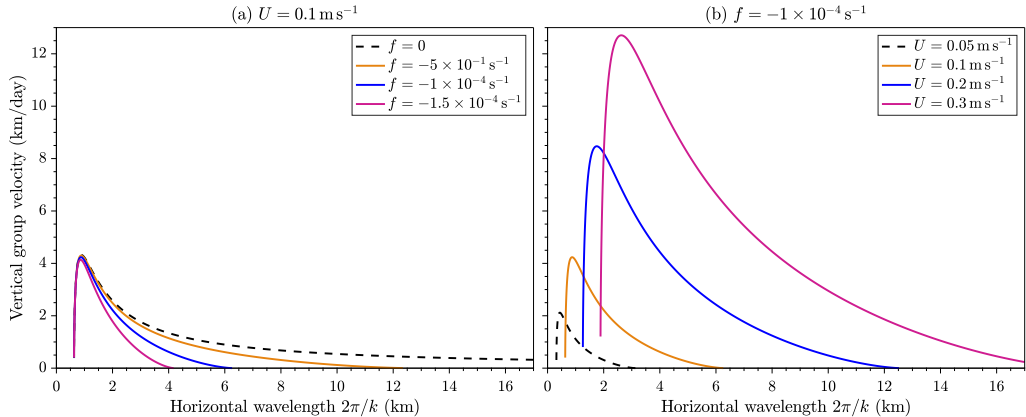


Figure 4: Vertical group velocity defined in (2.40) for the nonhydrostatic case and (a) fixed $U = 0.1 \text{ m s}^{-1}$, varying f and (b) fixed $f = -1 \times 10^{-4} \text{ s}^{-1}$, varying U , with $H = 3 \text{ km}$, $N = 1 \times 10^{-3} \text{ s}^{-1}$.

636 sharper horizontal gradients. The effect of rotation on larger scales significantly slows the
 637 vertical group velocity, so that larger horizontal scale waves will take significantly longer to
 638 develop. The group velocity increases with U , so larger background velocities allow faster
 639 lee wave propagation. For a wave with wavelength 3 km in a background flow $U = 0.1 \text{ m s}^{-1}$,
 640 $N = 1 \times 10^{-3} \text{ s}^{-1}$ and $f = -1 \times 10^{-4} \text{ s}^{-1}$, the vertical group velocity is approximately 1 km
 641 per day, suggesting that a wave would take 3 days to propagate to the surface and a further 3
 642 days to reflect back to the topography in an ocean of depth 3000 m. For a vertically varying
 643 background flow as is typical of the ocean, the vertical group velocity and wavelength will
 644 change during propagation, modifying this result. The timescale separation of full water-
 645 column lee wave formation and the mesoscale eddy field is therefore not clear, and depends
 646 on the scale of the waves. However, in energetic regions of the ocean such as the Drake
 647 Passage shown in figure 1, large velocities can enable high vertical group velocities and the
 648 steady approximation for lee waves at certain scales is expected to be valid.

649

2.10. Critical levels

650 In the inviscid and non-rotating problem, there are singularities of (2.13) - (2.15) at levels
 651 where $U = 0$ (Booker & Bretherton 1967; Maslowe 1986). These are known as critical
 652 levels, where the horizontal phase speed of the wave (here equal to zero) equals the mean
 653 flow speed. At these levels, the vertical wavelength and group velocity vanish. No energy
 654 or momentum flux at the original wavenumber can propagate any further vertically, and
 655 the perturbation velocities become very large, invalidating the linear solution. In reality,
 656 instabilities and energy loss can lead to wave breaking and reflection at this level (Wurtele
 657 1996), thus critical levels may be a sink of lee wave energy in the ocean (Bell 1975). However,
 658 this requires that the mean flow speed reaches zero somewhere in the water column. This is
 659 not an ubiquitous feature of the geostrophic eddies of the ACC, although critical levels may
 660 exist. This mechanism may be more important in regions of layered currents such as near the
 661 equator or in western boundary currents.

662 When rotation is included, there exist two further singularities of (2.13) at $U = \pm|f/k|$,
 663 above and below the critical level $U = 0$ (Jones 1967). These act to prevent the vertical
 664 propagation of the wavenumber k , in a similar way to the critical level of the non-rotating
 665 problem at $U = 0$. However, since each critical level is specific to the wavenumber k (unlike
 666 for the non-rotating problem), if the spectrum of the topography is continuous it can be

667 shown that there need not be singularities of the linear problem at these critical levels since
 668 the relevant solutions of (2.13) are logarithmic and thus integrable over a spectrum (Wurtele
 669 *et al.* 1996). Therefore, in reality there is not a single well defined critical level for lee waves
 670 with rotation and a continuous spectrum of wavenumbers. However, the solutions may still
 671 become nonlinear so as to invalidate the linear solution and cause breaking. It can also be
 672 shown that when $f \neq 0$, the solution at $U = 0$ is no longer singular (Grimshaw 1975) -
 673 physically this is because all components have already reached their first critical level and
 674 stopped propagating.

675 When the flow is sheared such that $|U|$ decreases with height, energy transfers from the lee
 676 waves to the mean flow via the E-P flux (see (2.46)), leaving less energy to be dissipated at the
 677 critical level for a particular wavenumber k . Kunze & Lien (2019) examine this mechanism
 678 as a possible sink for lee wave energy in regions of intensified bottom flow. In particular, for
 679 lee wave energy generated at wavenumbers far from the inertial limit $|Uk| = |f|$, a greater
 680 proportion of the initial energy is available to be reabsorbed by a mean flow decreasing with
 681 height, allowing a smaller percentage to be dissipated at the critical level at $|Uk| = |f|$ or
 682 elsewhere. For waves generated close to the inertial limit (from large scale topography), little
 683 energy is available for transfer to the mean flow, as it will instead soon reach its critical level
 684 and dissipate.

685 The inclusion of viscosity and diffusivity allows non-singular solutions to be found at
 686 critical levels where $|Uk| = |f|$. However, near these levels the wave fields can become
 687 nonlinear, invalidating the linear approach. Furthermore, on the approach to these levels the
 688 vertical wavelength tends to zero, creating sharp vertical gradients and enhancing energy
 689 loss. Having neglected vertical viscosity and diffusivity in our solution, this energy loss does
 690 not take place. When the horizontal viscosity and diffusivity are large enough and shear
 691 small enough for the solutions to stay appropriately linear as a critical level is approached,
 692 the linear solution is valid, but may be unrealistic due to the lack of vertical dissipation and
 693 mixing. Velocity profiles that decrease with height are therefore not considered hereafter.

694 For positively sheared background flows where the flow speed increases with height,
 695 energy instead transfers from the mean flow to the lee waves during propagation (see (2.46)).
 696 Since wind driven oceanic currents tend to be surface intensified, this may be a common
 697 occurrence. In this case (or if stratification N decreases with height), the waves may reach
 698 ‘turning levels’, whereby their intrinsic frequency $|Uk|$ reaches the buoyancy frequency N
 699 (Scorer 1949). At such levels the vertical wavenumber m tends to zero (see (2.18)), and the
 700 wave is reflected downward. Scorer (1949) showed that wave amplitudes in the resulting
 701 ‘trapped’ wave field could be increased by the superposition of reflected waves, much like
 702 in the current study due to the upper boundary. These turning levels are not the focus of our
 703 study, but may occur in the solutions for certain wavenumbers.

704

2.11. WKB solutions

705 Before solving the full equation (2.24) numerically, we first consider how much progress can
 706 be made with WKB theory (Gill 1982). Under the assumption that waves are propagating
 707 through a slowly varying medium such that the wavelength is small compared to the scale
 708 of changes in the background flow, WKB theory can often be used to find closed form
 709 solutions. In addition to the necessary assumption for linear theory that there are no critical
 710 levels (where $|U(z)k| = |f|$), WKB theory requires the further assumption that there are
 711 no turning levels (where $|U(z)k| = |N|$), since the vertical wavelength tends to infinity at
 712 these levels (see (2.18)). However, under the assumption that waves are generated and stay
 713 within the propagating range (2.19), solutions with both the rigid lid and freely radiating
 714 boundary condition can be found. For the latter, the component of the solution with positive
 715 local vertical group velocity is taken as in the uniform background case. de Marez *et al.*

716 (2020) find inviscid and non-rotating lee wave solutions under this approximation with a
 717 freely radiating boundary condition. Here, we extend their analysis to include rotation and
 718 viscous terms.

719 First, we write (for each k):

$$720 \quad \hat{\zeta}(z) = A(z)e^{i\varphi(z)}, \quad (2.52)$$

721 where $A(z)$ and $\varphi(z)$ are some real amplitude and phase such that $\varphi'(z) \sim m \sim 1/\lambda_z$, where
 722 λ_z is the vertical wavelength of the waves, itself varying over some lengthscale $L \gg \lambda_z$.
 723 $A(z)$ also varies on the lengthscale L due to changes in the background flow and to viscosity.
 724 At this point we must therefore also take the weakly viscous approximation $\mathcal{A}_h^2 k^2/U^2 \ll 1$
 725 to ensure that the decay scale due to viscosity is larger than the vertical wavelength of the
 726 waves (see (2.56) and discussion for justification). This is likely to be realistic in the ocean,
 727 as discussed after (2.49). Substituting (2.52) into (2.24), taking real and imaginary parts, and
 728 neglecting second order terms in λ_z/L allows two independent solutions to be found:

$$729 \quad \hat{\zeta}_{\pm}(k, z) = Q_r^{-\frac{1}{4}} e^{\int_0^z -\frac{1}{2}(P_r \pm Q_i/\sqrt{Q_r}) \pm i\sqrt{Q_r} d\hat{z}}, \quad (2.53)$$

730 where \hat{z} is a dummy integration variable, and Q_r, P_r and Q_i, P_i are the real and imaginary
 731 parts of P and Q , defined in (2.14) and (2.15). Setting $\mathcal{A}_h = \mathcal{D}_h$, and using the weakly
 732 viscous approximation, these become:

$$733 \quad Q_r = \frac{k^2(N^2 - \alpha U^2 k^2 - UU_{zz})}{U^2 k^2 - f^2}, \quad Q_i = \frac{\mathcal{A}_h k^3 [2Uk^2(N^2 - \alpha f^2) - U_{zz}(U^2 k^2 + f^2)]}{(U^2 k^2 - f^2)^2} \quad (2.54)$$

$$734 \quad P_r = \frac{2f^2 U_z}{U(U^2 k^2 - f^2)}, \quad P_i = \frac{2\mathcal{A}_h f^2 U_z k(3U^2 k^2 - f^2)}{U^2(U^2 k^2 - f^2)^2}. \quad (2.55)$$

736 Each term in (2.53) can be interpreted to understand the solutions. $Q_r^{-\frac{1}{4}} e^{-\frac{1}{2} \int_0^z P_r d\hat{z}}$ determines
 737 the change in amplitude of solution due to changes in the background flow, and is constant
 738 in a uniform flow. $e^{\mp \frac{1}{2} \int_0^z Q_i/\sqrt{Q_r} d\hat{z}}$ determines how the wave amplitude exponentially decays
 739 (or ‘grows’, for a downwards propagating component) due to viscosity. $e^{\pm i \int_0^z \sqrt{Q_r} d\hat{z}}$ is the
 740 oscillatory component, with wavenumber $\sim \sqrt{Q_r}$ (c.f. (2.17)).

741 The solution to the bounded problem can then be found using bottom and upper boundary
 742 conditions (2.25) and (2.37), and the solution to the unbounded problem can be found by
 743 taking $\zeta_{\pm}(k, z)$ (see discussion in §2.4.2) and using bottom boundary condition (2.25).

744 Simplifying further by considering the non-rotating and hydrostatic case with $f = \alpha = 0$,
 745 and assuming a linear velocity profile with $U_{zz} = 0$, the WKB solutions are given by:

$$746 \quad \hat{\zeta}_{\pm}(k, z) = \sqrt{\frac{U}{N}} e^{\pm \int_0^z \frac{N}{U} (i - \frac{\mathcal{A}_h k}{U}) d\hat{z}} \quad (2.56)$$

747 Aside from reflections and viscous dissipation, we expect that as U and N vary, $w \sim \hat{\zeta} \sim$
 748 $\sqrt{U/N}$, $u \sim \hat{\zeta}_z \sim \sqrt{N/U}$, and $\overline{uw} \sim$ constant, as expected by conservation of the E-P flux
 749 (2.50). The length scale of viscous decay is given by $U^2/\mathcal{A}_h N k$, and the ratio of the vertical
 750 wavelength to the viscous decay scale is $\mathcal{A}_h k/U$, justifying the condition $\mathcal{A}_h^2 k^2/U^2 \ll 1$ for
 751 use of the weakly viscous approximation.

752 Figure 5 shows the WKB non-hydrostatic, rotating, bounded solution for $\hat{\zeta}(k, z)$ and the
 753 corresponding full numerical solution (to be explained in §3) for three different values of k
 754 and various background profiles of $U(z)$ and $N(z)$. In figures 5a,c,d each of the wavenumbers
 755 k_1, k_2, k_3 remains within the propagating range (2.19) throughout the vertical domain, and the
 756 solutions are oscillatory. In each case, as k increases, the amplitude of the solutions decreases,

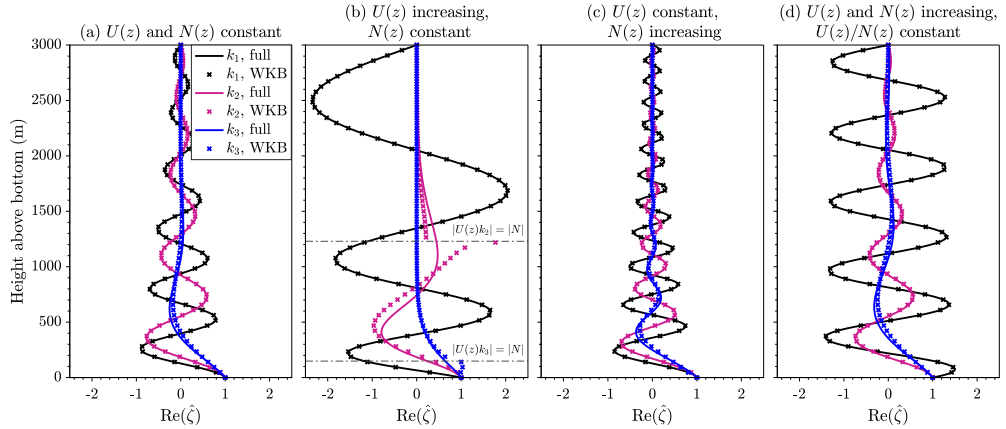


Figure 5: Numerical and WKB solutions $\Re[\zeta(\hat{k}, z)]$ to the rotating, nonhydrostatic, bounded problem defined in (2.24), with boundary conditions (2.25) and (2.37). Background fields vary linearly from $U(0) = 0.1 \text{ m s}^{-1}$ and $N(0) = 0.001 \text{ s}^{-1}$. a) $U(H) = U(0)$ and $N(H) = N(0)$, b) $U(H) = 0.3 \text{ m s}^{-1}$ and $N(H) = N(0)$, c) $U(H) = U(0)$ and $N(H) = 0.003 \text{ s}^{-1}$, and d) $U(H) = 0.3 \text{ m s}^{-1}$ and $N(H) = 0.003 \text{ s}^{-1}$. Solutions are shown at $k = \{k_1 = k_{\min} + 0.1(k_{\max} - k_{\min}), k_2 = 0.5 * (k_{\min} + k_{\max}), k_3 = k_{\max} - 0.1(k_{\max} - k_{\min})\}$, where $k_{\min} = f/U(0)$, $k_{\max} = N(0)/U(0)$, and $f = -1 \times 10^{-4} \text{ s}^{-1}$.

757 since the length scale of viscous decay decreases (c.f. (2.56)). The exponential decay when
 758 $k = k_3$ (blue lines) is large enough that oscillatory component is small in comparison.

759 In general, the numerical and WKB solutions agree well, although to a lesser extent as
 760 k increases since m decreases (c.f. (2.18)), and thus λ_z increases, invalidating the WKB
 761 approximation. In figure 5b $U(z)$ increases and the solutions do not all stay within in the
 762 propagating range (2.19). Components k_2 and k_3 reach their turning levels where $|Uk| = |N|$,
 763 and the WKB approximation is not valid for these solutions.

764 Comparing the $k = k_1$ component in figure 5a (constant background fields) with figures
 765 5b (U increasing) and 5c (N increasing), we see that the scalings inferred from (2.53) hold,
 766 and the amplitude of $\hat{\zeta}$ (and w) increases with increasing U and decreases with increasing
 767 N . The vertical wavelengths scale with U/N , although they are also dependent on k , as is
 768 expected from (2.18).

769 A further observation from figures 5a,d is the reduced impact of viscosity and larger
 770 amplitudes when U and N increase together, even though U/N is fixed. This is because the
 771 vertical group velocity of the waves is larger in this case - from (2.40) we can see that for
 772 $f^2 \ll U^2 k^2 \ll N^2$, the vertical group velocity $\sim U^2 k/N$. The waves have therefore decayed
 773 less by the time they reach and reflect from the surface. Equivalently, the decay scale due to
 774 viscous dissipation $U^2/\mathcal{A}_h N k$ increases with U even when U/N is fixed.

775 The WKB solutions are insightful provided there are no turning levels, and offer closed
 776 form solutions and insights that are not available from the numerical solutions. Similar
 777 approximations could also be made to implement a vertical and/or vertically variable
 778 viscosity, although we do not pursue this here to avoid further complexity. WKB solutions
 779 may therefore be more useful than numerical solutions in any eventual parametrisation of
 780 this process. However, hereafter we employ the full numerical solution, with no assumptions
 781 on the lengthscale of variations of the background flow or the viscous decay scale in order
 782 to study a wider range of wavenumbers and background flows.

783

784 3. Numerical solution

785 The full solution to the viscous linear lee wave problem will be found subject to both the
 786 radiating upper boundary condition (in which case we require U and N to be constant with
 787 height, as discussed in §2.4) and the rigid lid upper boundary condition, in which case we
 788 consider general $N^2 > 0$ and $U(z)$ such that $U > 0$, $U_z > 0$ and $fU_{zz} = 0$ (see §2.1).

789 3.1. Unbounded solver

790 The solution can be found in the traditional way (Bell 1975), with the requirement the solution
 791 decays away from the topography as discussed in §2.4. The solution for ψ is given by (2.23),
 792 where $\hat{\zeta}(k, z)$ satisfies (2.24) - (2.25), with the radiating upper boundary condition satisfied
 793 by taking the correct choice of branch for m . Note that $P(k, z) = 0$ and $Q(k, z) = Q(k)$, so
 794 the solution for $\hat{\zeta}$ is simply:

$$795 \quad \hat{\zeta}(k, z) = e^{im(k)z}, \quad (3.1)$$

796 where $m^2(k) = Q(k)$ and $\Im(m) > 0$. This can be implemented numerically for general
 797 topography $h(x)$ by performing the Fourier transforms with a FFT. Once ψ is found, all other
 798 wave fields can be recovered.

799 3.2. Bounded solver

800 When the background flow is uniform in z , the solutions can be found similarly to the
 801 unbounded case above, using the analytic solution (2.42) for $\hat{\zeta}(k, z)$. When U and N are not
 802 uniform, we use Galerkin methods to solve (2.24) - (2.37), an unforced second order ordinary
 803 differential equation with inhomogeneous boundary conditions. First, we transform it into a
 804 forced problem with homogeneous boundary conditions. Let

$$805 \quad \hat{\zeta}(k, z) = \hat{\phi}(k, z) + G(k, z), \quad (3.2)$$

806 where G is some function such that $G(k, 0) = 1$ and $G(k, H) = 0$. Then $\hat{\phi}$ satisfies

$$807 \quad \hat{\phi}_{zz} + P(k, z)\hat{\phi}_z + Q(k, z)\hat{\phi} = R(k, z), \quad (3.3)$$

$$808 \quad \hat{\phi}(k, 0) = 0, \quad (3.4)$$

$$809 \quad \hat{\phi}(k, H) = 0, \quad (3.5)$$

810 and R satisfies

$$812 \quad G_{zz} + P(k, z)G_z + Q(k, z)G = -R(k, z). \quad (3.6)$$

813 G can be chosen to be any function satisfying $G(k, 0) = 1$ and $G(k, H) = 0$. We choose it
 814 so that $R(k, 0) = R(k, H) = 0$ by taking G to be a cubic polynomial in z , and solving for
 815 the coefficients. R can then be found via (3.6). The problem (3.3) - (3.5) can now be solved
 816 numerically using Galerkin methods. Specifically, for each k we decompose $\hat{\phi}$, P , Q , and R
 817 into finite Fourier sums with some truncation limit M :

$$818 \quad \hat{\phi}(k, z) = \sum_{s=1}^M a_s(k) \sin \frac{s\pi z}{H}, \quad P(k, z) = \sum_{j=1}^M p_j(k) \sin \frac{(j-1)\pi z}{H},$$

$$819 \quad Q(k, z) = \sum_{i=1}^M q_i(k) \cos \frac{(i-1)\pi z}{H}, \quad R(k, z) = \sum_{n=1}^M r_n(k) \sin \frac{(n-1)\pi z}{H}, \quad (3.7)$$

820 where the q_i , p_j and r_n are known and found via the relevant sine or cosine transform, and
 821 the coefficients a_s are to be found. Notice that the sine expansion of $\hat{\phi}$ and R ensures that

823 their boundary conditions are satisfied. However, if $P \neq 0$ or $Q_z \neq 0$ at $z = 0, H$, the sine and
 824 cosine expansions of P and Q respectively must represent one or more discontinuities in P
 825 or Q_z at endpoints. The numerical solution is therefore an approximation that is valid only in
 826 the interior, although (3.3) is satisfied everywhere by the series expansions. There can also be
 827 noise at the frequency of the truncation limit near the endpoints of the series representations
 828 due to the Gibbs phenomenon. With increasing truncation limit and vertical resolution, the
 829 interior series solution approaches the actual solution at all interior points - (2.46) can be
 830 used to validate this. As a consequence, quantities should be evaluated with care at $z = 0, H$,
 831 and (2.51) is used to find the wave drag rather than direct evaluation at $z = 0$.

832 Substituting (3.7) into (3.3), integrating over $z \in [0, H]$ and using the orthogonality
 833 properties of sine and cosine gives a matrix equation for the coefficients a_s :

$$834 \quad A_{sn}a_n = B_{sn}r_n, \quad (3.8)$$

835 where:

$$836 \quad A_{sn} = -\left(\frac{n\pi}{H}\right)^2 \delta_{s,n} + \frac{n\pi}{2H}(p_{s-n+1} + p_{s+n+1} - p_{n-s+1}) + \frac{1}{2}(q_{s-n+1} + q_{n-s+1} - q_{s+n+1}), \quad (3.9)$$

$$837 \quad B_{sn} = \delta_{n,s+1}. \quad (3.10)$$

839 The a_s can now be found from (3.8) by inverting the matrix A . $\hat{\phi}$ can then be recovered from
 840 the coefficients a_s , $\hat{\zeta}$ found from (3.2), and $\hat{\psi}$ found from (2.23).

841 3.3. Topography

842 The topography is found from the theoretical abyssal hill topographic spectrum proposed
 843 by Goff & Jordan (1988), and is similar to that used in previous lee wave modelling
 844 studies (Nikurashin & Ferrari 2010b, 2011; Nikurashin *et al.* 2014; Klymak 2018; Zheng
 845 & Nikurashin 2019). This choice allows both comparison to the results of these studies,
 846 and consideration of the behaviour of a range of different wavenumbers without expanding
 847 the parameter space of investigation. The 1D topography is found from the theoretical
 848 topographic spectrum $P_{2D}(k, l)$:

$$849 \quad P_{2D}(k, l) = \frac{2\pi h_0^2(\mu - 2)}{k_0 l_0} \left(1 + \frac{k^2}{k_0^2} + \frac{l^2}{l_0^2}\right)^{-\frac{\mu}{2}}, \quad (3.11)$$

850 by integrating over wavenumbers l . k_0 and l_0 are the characteristic horizontal wavenumbers, μ
 851 is the high wavenumber spectral slope, and h_0 is the RMS abyssal hill height. For comparison
 852 with other recent lee wave studies, we set $k_0 = 2.3 \times 10^{-4} \text{ m}^{-1}$, $l_0 = 1.3 \times 10^{-4} \text{ m}^{-1}$ and
 853 $\mu = 3.5$, in line with representative parameters of the Drake Passage region used in Nikurashin
 854 & Ferrari (2010a); Zheng & Nikurashin (2019). Next, $P_{1D}(k)$ is set to zero for wavenumbers
 855 k such that $|U(0)k| < |f|$ or $|U(0)k| > |N(0)|$, since solutions in these ranges are non-
 856 propagating. The typical values used are $N(0) = 1 \times 10^{-3} \text{ s}^{-1}$, $U(0) = 0.1 \text{ m s}^{-1}$ and $f =$
 857 $-1 \times 10^{-4} \text{ s}^{-1}$, corresponding to a topography with wavelengths between $\sim 630 \text{ m}$ and \sim
 858 6300 m . Note that the same topography is used throughout, even when $f = 0$.

859 The topographic height differs from that used in the aforementioned studies, since the
 860 solver is linear and the solutions must therefore remain approximately linear to be valid.
 861 We normalise the topography resulting from the above steps so that the RMS of the final
 862 topography $h_{rms} = 25 \text{ m}$. This gives a Froude number $Fr_L = Nh_{rms}/U = 0.25$ and is
 863 sufficient to keep the solution near linear such that the perturbation horizontal velocity u
 864 is less than the background velocity U , with the exception of resonant cases. This is an

865 unrealistically low Froude number for the rough topography of many parts of the Southern
 866 Ocean (Nikurashin & Ferrari 2010a), but since the perturbation quantities are linear in $\hat{h}(k)$
 867 (e.g. (2.23)), simple scaling arguments can recover the dependence on h_{rms} . The goal of this
 868 study is not to make predictions of the actual magnitude of the lee wave field, but its structure
 869 in the vertical and dependence on viscosity and diffusivity, background fields, and boundary
 870 condition.

871

3.4. Numerical set-up

872 In the following section, the numerical solver is used to solve for the wave fields in a 2D
 873 domain of width 40 km, and height 3 km. The number of gridpoints in x and k is 800, and in
 874 z is 257. The truncation limit M (see (3.7)) is 200. Sensitivity tests were performed to ensure
 875 that increasing these resolutions does not impact the results.

876 The horizontal Prandtl number $Pr_h = \mathcal{A}_h/\mathcal{D}_h$ is assumed to be equal to one throughout
 877 - Shakespeare & Hogg (2017) discuss the effect of non-zero Prandtl number on lee waves.
 878 Hereafter, we refer only to the viscosity \mathcal{A}_h , with the understanding that the diffusivity \mathcal{D}_h
 879 varies similarly.

880 4. Results

881 Results from the numerical solvers are now presented. First, the hydrostatic and non-rotating
 882 solution is shown to demonstrate the resonance and modification of generation that occurs
 883 when the horizontal group velocity is zero, as described in §2.5 and §2.7. Next, nonhydrostatic
 884 effects and rotation are introduced to the solution, and the results compared to the previous
 885 case. Finally, the effects of non-uniform stratification and velocity are shown.

886

4.1. Hydrostatic and non-rotating solutions

887 Figures 6a,b show the numerical linear solution for the vertical velocity field under the
 888 hydrostatic and non-rotating approximations with viscosity $\mathcal{A}_h = 1 \text{ m}^2 \text{ s}^{-1}$. In figure 6a,
 889 there is an open boundary (OB) and waves can freely propagate out of the domain, whereas
 890 in figure 6b the rigid lid (RL) boundary condition is implemented. The reflection of waves and
 891 superposition back onto the wave field is clear, as is the well defined vertical wavenumber
 892 $m \sim N/U = 0.01 \text{ m}^{-1}$, giving a vertical wavelength of $2\pi/m \sim 628 \text{ m}$. As discussed in
 893 §2.5, when $f = \alpha = 0$, the horizontal component of group velocity is zero, as can be
 894 seen in the vertically radiating waves in figures 6a,b. As a result, waves reflected at the
 895 surface superimpose directly back onto the original wave field. Notice that near topography
 896 the solutions in figures 6a,b are similar since energy has been lost in the reflected wave,
 897 thus the solution consists mostly of the original upwards propagating component. This is
 898 also somewhat visible in figure 6c, which shows the difference between the bounded and
 899 unbounded solutions - the greatest differences are seen near the surface.

900 Section 2.7 describes how resonance can occur when $N^2 H^2 / U^2 = n^2 \pi^2$, $n \in \mathbb{N}$, in the
 901 inviscid, non-rotating, hydrostatic scenario. Figure 7 demonstrates this phenomenon with the
 902 given topography spectrum for varying viscosity \mathcal{A}_h . Figure 7a shows the lee wave energy
 903 flux at $z = 0, 1000 \text{ m}$, and H for the OB and RL solutions with $H = 9.95\pi U/N \simeq 3126 \text{ m}$
 904 (constructive interference) and $H = 9.5\pi U/N \simeq 2985 \text{ m}$ (destructive interference). For the
 905 OB solution the energy flux at $z = 0$ is almost independent of viscosity - it is modified slightly
 906 by the local viscous term at $z = 0$ (not shown hereafter), but not the viscosity elsewhere in
 907 the domain since energy can only radiate away from the topography. As viscosity increases,
 908 the energy flux at $z = 1000 \text{ m}$ and the surface decreases as more energy is lost during
 909 propagation. At $\mathcal{A}_h = 1 \text{ m}^2 \text{ s}^{-1}$, approximately 40% of the wave energy dissipates in the
 910 bottom 1000 m.

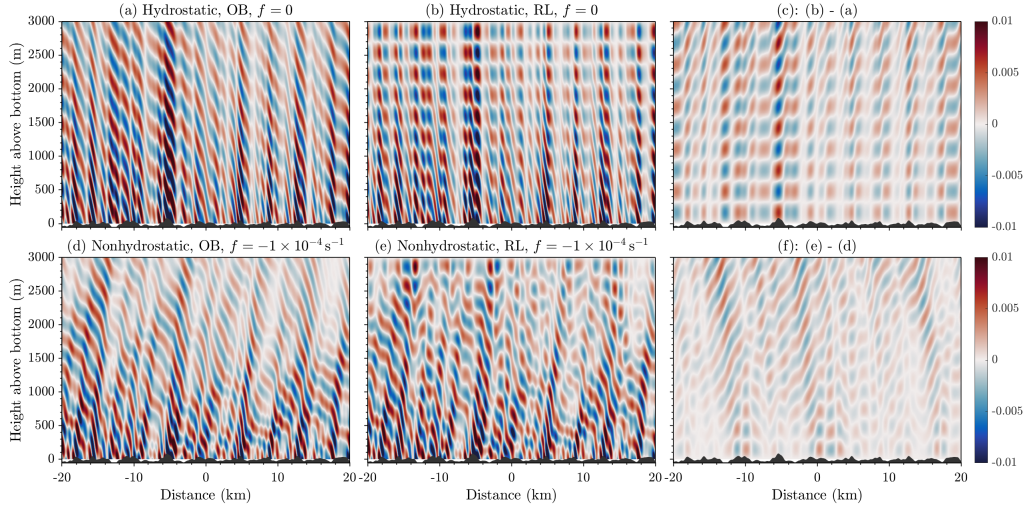


Figure 6: Vertical velocity (m s^{-1}) from the linear solver (a) with an open boundary (OB), $f = 0$, hydrostatic, (b) with a rigid lid (RL), $f = 0$, hydrostatic, (c) the difference between (b) and (a), (d) with an open boundary (OB), $f = -1 \times 10^{-4} \text{ s}^{-1}$, nonhydrostatic, (e) with a rigid lid (RL), $f = -1 \times 10^{-4} \text{ s}^{-1}$, nonhydrostatic, and (f) the difference between (e) and (d). $\mathcal{A}_h = 1 \text{ m}^2 \text{ s}^{-1}$, $U = 0.1 \text{ m s}^{-1}$, $N = 1 \times 10^{-3} \text{ s}^{-1}$ for all cases. Topography $h(x)$ is shown, although it is applied in the linear approximation at its mean value of $z = 0$.

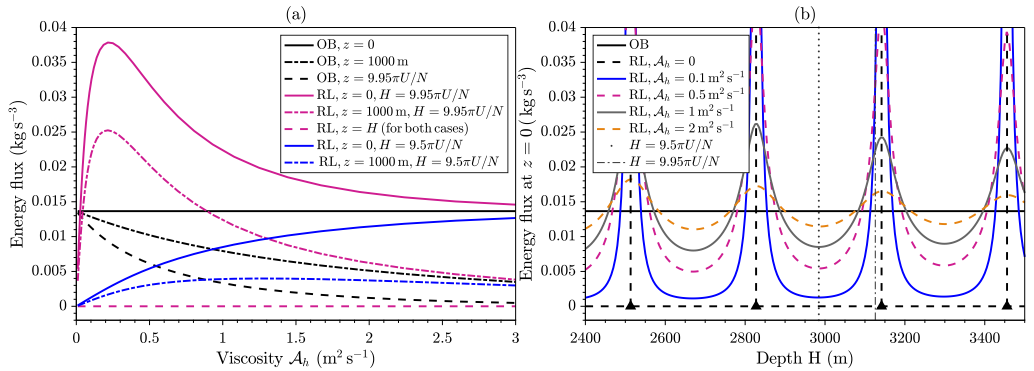


Figure 7: (a) Horizontally averaged vertical energy flux at various heights for the open boundary (OB) and rigid lid (RL) hydrostatic and non-rotating solvers, against horizontal viscosity \mathcal{A}_h . (b) Horizontally averaged vertical energy flux at $z = 0$ (proportional to wave drag) for several values of viscosity \mathcal{A}_h against ocean depth H . Vertical dashed lines and triangles indicate the singularities $N^2 H^2 / U^2 = n^2 \pi^2$, $n = 8, 9, 10, 11$. Other vertical lines indicate the values of H shown in (a). $U = 0.1 \text{ m s}^{-1}$, $N = 1 \times 10^{-3} \text{ s}^{-1}$, $f = 0$ in both.

911 For the RL solver, the results are markedly different for the two different domain heights
 912 H . In both cases, the energy flux is zero at $z = H$ due to the boundary condition, and zero
 913 when $\mathcal{A}_h = 0$, since there can be no steady state energy flux into lee waves without mixing
 914 and dissipation (see (2.51)). Equivalently, all upwards propagating energy flux is cancelled
 915 out by the reflected downwards component. However, for the near resonant case, when a
 916 small value of viscosity $\mathcal{A}_h = 0.25 \text{ m}^2 \text{ s}^{-1}$ is introduced the energy flux at the topography
 917 increases to over 2.5 times that with no upper boundary. Now that there is no longer exact
 918 cancellation of the energy flux, constructive interference of the wave field initially allows the

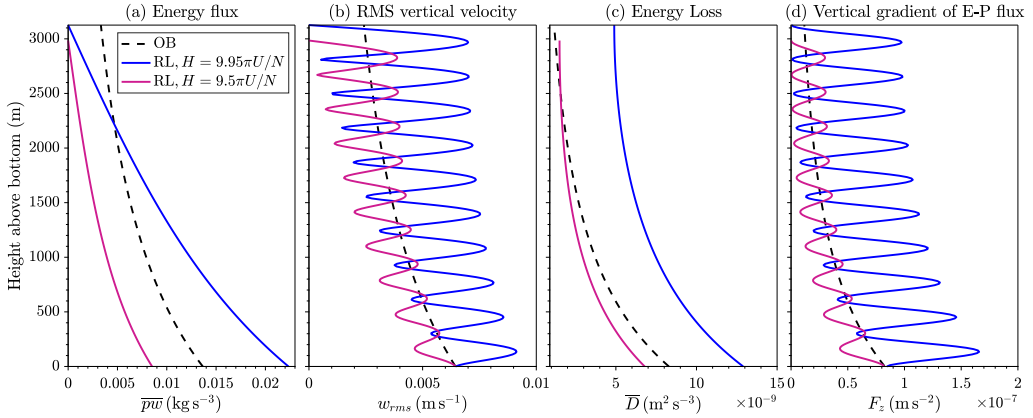


Figure 8: Horizontally averaged (a) energy flux (b) RMS vertical velocity, (c) energy loss, (d) vertical gradient of the E-P flux as a function of z for the open boundary (OB) solver and the rigid lid (RL) solver with constructive and destructive interference. $\mathcal{A}_h = 1 \text{ m}^2 \text{ s}^{-1}$, $f = 0$, $U = 0.1 \text{ m s}^{-1}$, $N = 1 \times 10^{-3} \text{ s}^{-1}$.

919 energy flux to increase with increasing \mathcal{A}_h . As viscosity increases further, energy loss of the
 920 reflected wave reduces the constructive interference and the energy flux at $z = 0$ decreases,
 921 approaching that of the unbounded solution until it no longer ‘knows about’ the boundary.
 922 The energy flux at $z = 1000 \text{ m}$ follows a similar pattern, approaching the OB flux as \mathcal{A}_h
 923 increases.

924 In contrast, the energy flux in the RL solution with $H = 9.5\pi U/N$ remains smaller than
 925 that in the OB solution throughout, since the effect of the boundary is to produce destructive
 926 interference with the original wave field. When the energy flux at $z = 0$ from the solution
 927 with constructive interference peaks at $\mathcal{A}_h = 0.25 \text{ m}^2 \text{ s}^{-1}$, the energy flux from the solution
 928 with destructive interference is ~ 13 times smaller.

929 Figure 7b demonstrates this constructive/destructive behaviour of the wave field as H
 930 varies. Again, the OB energy flux at $z = 0$ is almost constant with changes in \mathcal{A}_h and constant
 931 with changes in H . The RL energy flux at $z = 0$ for $\mathcal{A}_h = 0$ is shown in black dashes, with the
 932 triangles and asymptotes indicating the singularities at $N^2 H^2 / U^2 = n^2 \pi^2$, $n = 8, 9, 10, 11$.
 933 When $\mathcal{A}_h \neq 0$, the solutions become continuous with peaks at the singularities (constructive
 934 interference) and troughs halfway between (destructive interference). As \mathcal{A}_h increases, the
 935 energy flux approaches the constant value of the OB solution. The values of H in figure 7a
 936 are shown as vertical lines in figure 7b.

937 The vertical structure of the energy flux, RMS vertical velocity, energy loss, and vertical
 938 gradient of the E-P flux are shown in figure 8 for the same cases described in figure 7
 939 at $\mathcal{A}_h = 1 \text{ m}^2 \text{ s}^{-1}$. Figure 8a again demonstrates the difference in energy fluxes with the
 940 boundary condition and height of domain. Figure 8b shows a periodic vertical structure in
 941 the RMS vertical velocity w_{rms} of the RL solutions that does not exist in the OB solution,
 942 due to the superposition of upwards and downwards propagating waves. This has the effect
 943 of enhancing the maximum w_{rms} over a vertical wavelength, and decreasing the minimum,
 944 so that even in the destructive interference case where the energy flux in the RL solution
 945 is significantly smaller than the OB solution, the peak w_{rms} is larger than that of the OB
 946 solution.

947 The energy loss \bar{D} (the sum of mixing and dissipation rate) is shown in figure 8c. In the
 948 RL case the vertical phases of the waves are aligned due to the surface boundary condition,
 949 and the mixing and dissipation rate individually have a sinusoidal structure out of phase with

each other (not shown). This is due to the energy distribution in the wave alternating between kinetic and potential over a vertical wavelength. There is over 2.5 times more energy loss in total when $H = 9.95\pi U/N$ (constructive interference) compared to when $H = 9.5\pi U/N$ (destructive interference). Comparing the OB and RL solutions for $H = 9.5\pi U/N$, it can be seen that energy loss in the RL solution is enhanced near the surface, suggesting that the upper boundary moves the distribution of wave energy (and therefore energy loss) higher up in the water column.

The vertical gradient of the E-P flux is shown in figure 8d, representing the force on the flow due to wave breaking. In the RL cases, F_z has a periodic structure in the vertical due to the wave interference, which would impact the feedback of the waves on the mean flow. The vertical integral of F_z gives the total wave drag on the flow, hence the constructive interference produces a high drag state and the destructive interference a low drag state.

4.2. Nonhydrostatic and rotating solutions

When rotation ($f \neq 0$) and nonhydrostatic ($\alpha = 1$ in (2.9)) effects are introduced, the resonance and interference effects described in §4.1 are no longer as straightforward. As shown in §2.5, the horizontal component of the group velocity is now positive, allowing wave energy to travel downstream. Figures 6d,e show the vertical velocity field for the same background flow conditions and topography as figures 6a,b, but now with $f = -1 \times 10^{-4} \text{ s}^{-1}$ and $\alpha = 1$. Waves now propagate downstream as well as vertically, and the resulting structure in the RL solution (figure 6e) is not as simple. However, the characteristic vertical phase lines and modal structure of the disturbances just below the surface caused by superposition of the reflected waves remain.

Rotation reduces the generation of larger horizontal scale waves (e.g. figure 4a), and the dominant components of the wave field are therefore more easily dissipated than in the non-rotating solution shown in figures 6a,b. The vertical group velocity is also reduced by rotation (figure 4a), so the waves radiate more slowly away from the topography and lose more energy before reaching the surface. The wave field in the lower part of the domain of figure 6e therefore resembles the OB solution in figure 6d more closely than in the non-rotating solution, since the dominant wavelengths have lost more energy by the time they return to the topography. The similarity of these two fields near the topography can be seen in figure 6f, which shows the difference between figures 6e and 6d.

Figure 9 shows the same data as figure 7, now with rotation and nonhydrostaticity included, for two domain heights H that have been picked to represent constructive and destructive interference of the new system. It is clear from figure 9b that the simple hydrostatic resonance has been replaced by multiple resonances where $|m(k)H| \simeq n\pi$ (c.f. (2.43)) for some $n \in \mathbb{N}$ and some k in the spectrum $\hat{h}(k)$. As H varies, the energy flux at the topography varies erratically as different wavenumbers k in the topographic spectrum interfere constructively and destructively, with energy flux tending to that of the OB solution as \mathcal{A}_h increases. The example values of H in figure 9a are shown as vertical lines in figure 9b. At $H = 3015 \text{ m}$ there is net destructive interference, and energy fluxes are below those of the OB solution, whereas at $H = 2982 \text{ m}$ there is net constructive interference, and the energy flux is higher than the OB solution. The RL solutions tend to the OB solutions with increasing \mathcal{A}_h more quickly in figure 9a than in figure 7a, since the dominant wavelengths are shorter and decay faster.

Importantly, since the horizontal group velocities are now positive so that the reflected wave does not directly superimpose onto the upwards propagating wave, the main reason for the modification of the bottom energy flux (and wave drag) with a reflecting upper boundary is the periodic nature of the topography used. The overlap parameter (defined in (2.41)) for this set of parameters is above 2 for all wavenumbers (orange line in figure 3b). If the

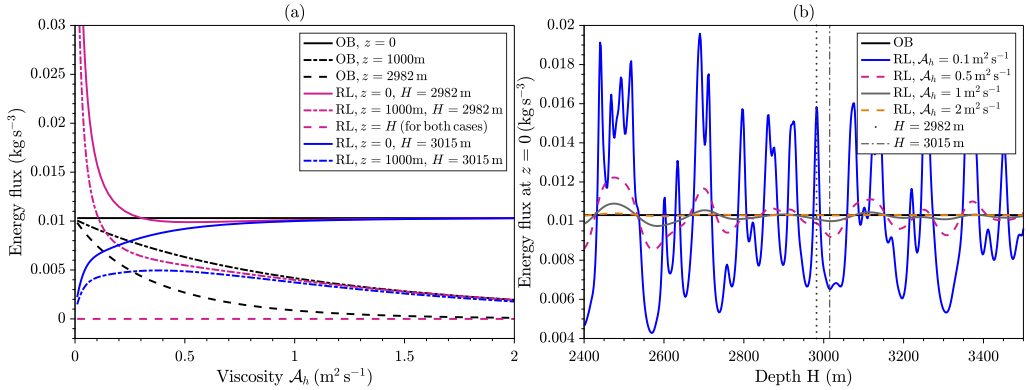


Figure 9: Same as figure 7, for the non-hydrostatic and rotating case with $f = -1 \times 10^{-4} \text{ s}^{-1}$. Vertical lines in (b) indicate the values of H shown in (a). Note that the domain heights H picked to represent constructive and destructive interference of the system have changed.

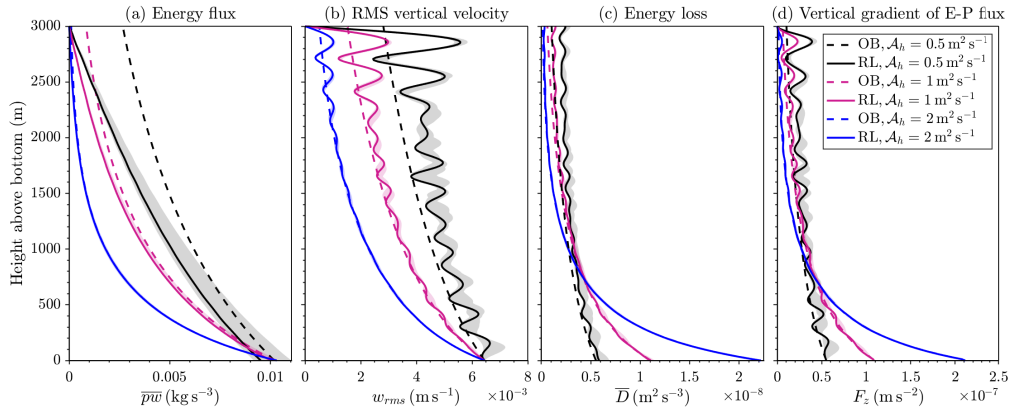


Figure 10: Same as figure 8, for the nonhydrostatic and rotating case at various \mathcal{A}_h . Results from the RL solver are shown as a range (shaded) of solutions with $H = 2900$ to 3100 m (with axes scaled onto $z \in [0, 3000]$ m] to show the effect of constructive/destructive interference, and in solid for $H = 3000$ m. $f = -1 \times 10^{-4} \text{ s}^{-1}$, $U = 0.1 \text{ m s}^{-1}$, $N = 1 \times 10^{-3} \text{ s}^{-1}$.

999 topography were isolated, the bottom energy flux may not be changed at all, dependent on
 1000 the relevant overlap parameter. Even when there are near-resonances caused by constructive
 1001 interference (peaks in figure 9b), they are smaller in amplitude than those in the hydrostatic,
 1002 non-rotating case (figure 7b) since the waves are dispersive, and the resonances occur for
 1003 individual wavenumbers rather than the whole wave field.

1004 From figure 9b, it is clear that even with periodic topography, when $\mathcal{A}_h \gtrsim 0.5 \text{ m}^2 \text{ s}^{-1}$, the
 1005 constructive and destructive interferences with varying H do not greatly affect the bottom
 1006 energy flux; for $H > 3000$ m the change from the open boundary case is less than 10%. H
 1007 is hereafter set to 3000 m, although shaded regions in figures 10, 12, 13, 14 and 16 show the
 1008 range of solutions for H between 2900 m and 3100 m (with axes scaled onto $[0, 3000]$ m], to
 1009 indicate the extent of the interference. Figure 10 shows the vertical structure of the fields as
 1010 in figure 8 for the nonhydrostatic and rotating RL and OB solutions at various values of \mathcal{A}_h .
 1011 The profiles of energy flux in figure 10a show, as expected, that the RL solution approaches

1012 the OB solution as \mathcal{A}_h increases. They will be identical when the energy flux at $z = H$ in the
 1013 OB solution is zero.

1014 As was found in the hydrostatic and non-rotating case in figure 8b, RMS vertical velocity
 1015 profiles shown in figure 10b are generally enhanced for the RL compared to the OB solution.
 1016 w_{rms} oscillates in z due to the constructive and destructive interference of the wave field,
 1017 with the maxima significantly larger than the OB solution, and the minima often larger
 1018 too, especially in the lower viscosity cases. In particular, the subsurface maxima (located
 1019 approximately $\pi U/2N \simeq 157$ m below the surface) are significantly larger than the OB
 1020 solution at that level, 1.8 – 1.9 times larger for each of the values of \mathcal{A}_h shown here. They
 1021 are also larger than the next deeper maximum below for each \mathcal{A}_h , and even larger than the
 1022 RMS vertical velocities down to $z = 700$ m for $\mathcal{A}_h = 0.5 \text{ m}^2 \text{ s}^{-1}$. The effect of the boundary
 1023 is clearly to enhance the RMS vertical velocity in the upper ocean.

1024 The energy loss shown in figure 10c is larger in the RL case than in the OB case for each
 1025 value of \mathcal{A}_h . This is expected, since energy leaves the domain in the OB case, but must stay
 1026 in the domain and be dissipated in the RL case. There is a subtlety in that in the RL case
 1027 the bottom energy flux itself can be modified (see shading in figure 10a, and figure 9b and
 1028 discussion), however the effect is not significant here. Consistent with the results of Zheng
 1029 & Nikurashin (2019), we find that the total energy loss over the water column is increased
 1030 from the OB case, though the difference is not large, between 1% for $\mathcal{A}_h = 2 \text{ m}^2 \text{ s}^{-1}$ and
 1031 26% for $\mathcal{A}_h = 0.5 \text{ m}^2 \text{ s}^{-1}$. Assuming that the energy flux at the topography is unchanged by
 1032 reflections, since U is uniform with height the total energy loss for each case in figure 10c
 1033 must be the same (see (2.51)) - but the OB solutions must be integrated to an infinite height
 1034 to get this result. The main result of note is the difference in the distribution of energy loss in
 1035 the water column when a RL is introduced - it is skewed towards the surface, with an increase
 1036 of 45% for $\mathcal{A}_h = 2 \text{ m}^2 \text{ s}^{-1}$ and 70% for $\mathcal{A}_h = 0.5 \text{ m}^2 \text{ s}^{-1}$ in the top 1000 m compared to the
 1037 OB case. Of course, these results are sensitive to the choice of ocean depth used, since in the
 1038 limit $H \rightarrow \infty$ the RL and OB cases will be identical (excepting the perfectly inviscid case).
 1039 For greater depths H , the differences reported in the top 1000 m will be less pronounced.

1040 The gradient of the E-P flux (figure 10d) has a similar structure to the energy loss (figure
 1041 10c). This is because U is constant with height, and neglecting the effect of the upper
 1042 boundary, both wave energy flux (the gradient of which for U constant is given by \bar{D} from
 1043 (2.46)) and the E-P flux (with gradient F_z) decrease only due to mixing and dissipation.
 1044 Equivalently to noting as above that the total height integrated energy loss should be the
 1045 same, the total wave drag on the flow, given by the integral of F_z , should also be the same
 1046 for the cases shown, though when restricting to $z \in [0, 3000 \text{ m}]$ the total wave drag in the RL
 1047 solutions is larger than that of the OB solutions.

1048 For idealised, nonlinear, 2D, open boundary simulations with a similar topographic
 1049 spectrum and flow parameters, Nikurashin & Ferrari (2010b) found that $\sim 10\%$ of lee
 1050 wave energy dissipated in the bottom 1 km for $Fr_L = 0.2$, and $\sim 50\%$ for $Fr_L \geq 0.5$
 1051 (representative of the Drake Passage). From the black dot-dashed line in figure 9a, these
 1052 regimes would equate to $\mathcal{A}_h = 0.2 \text{ m}^2 \text{ s}^{-1}$ and $0.7 \text{ m}^2 \text{ s}^{-1}$ respectively here. Of course,
 1053 the change in implied turbulent viscosity between the two regimes is largely down to the
 1054 nonlinearity and subsequent breaking for higher Froude number. This suggests that if a linear
 1055 solution with a constant turbulent viscosity is to have any success in practise, it must be
 1056 adjusted for the actual nonlinearity of the waves.

1057 Comparing the energy loss (figure 10c) with the common parametrisation for the expo-
 1058 nential vertical decay of lee wave energy dissipation (Nikurashin & Ferrari 2013; Melet
 1059 *et al.* 2014), the decay scale for the OB solver (calculated as the height above bottom at
 1060 which energy loss is equal to e^{-1} times its bottom value) is approximately 1700 m for

1061 $\mathcal{A}_h = 0.5 \text{ m}^2 \text{ s}^{-1}$, 800 m for $\mathcal{A}_h = 1 \text{ m}^2 \text{ s}^{-1}$, and 400 m for $\mathcal{A}_h = 2 \text{ m}^2 \text{ s}^{-1}$. Proposed
 1062 values of the lee wave decay scale (Nikurashin & Ferrari 2013) range between 300 m and
 1063 1000 m. This together with the comparison of the energy flux to the nonlinear simulations
 1064 of Nikurashin & Ferrari (2010b) suggests that we are in the correct parameter space for \mathcal{A}_h ,
 1065 and therefore that the upper boundary could have an influence on the wave field. We hereafter
 1066 show results for $\mathcal{A}_h = 0.5$ and $1 \text{ m}^2 \text{ s}^{-1}$.

1067

4.3. Non-uniform velocity and stratification

1068 In reality, the assumption that background flow is uniform with height is unlikely to be
 1069 valid when considering lee wave propagation throughout the entire water column. We now
 1070 consider the impact of varying $U(z)$ and $N(z)$ on the lee wave field.

1071 Unlike in the unbounded case, when solving the lee wave problem with a rigid lid upper
 1072 boundary it is straightforward to solve with arbitrary mean flow velocity and stratification.
 1073 Some constraints do apply, and we only consider velocity profiles $U(z) > 0$ such that
 1074 $fU_{zz}(z) = 0$, so that the base state is effectively 2D (see §2.1), and $U'(z) > 0$, to avoid
 1075 difficulties with critical levels (see §2.10). Typical oceanic conditions are characterised by
 1076 lower velocities at depth and larger velocities at the surface, so this scenario is realistic,
 1077 although lee wave generation at locations of intensified bottom velocities may also be
 1078 important (Kunze & Lien 2019). The only constraint on the stratification N^2 is that $N^2 \geq 0$
 1079 so that the mean flow is statically stable.

1080 First, U is varied linearly from $U(0) = 0.1 \text{ m s}^{-1}$ to $U(H) = 0.1, 0.2$ or 0.3 m s^{-1} with
 1081 $N = 1 \times 10^{-3} \text{ s}^{-1}$ and $\mathcal{A}_h = 0.5$ and $1 \text{ m}^2 \text{ s}^{-1}$. The vertical velocity fields when $U(H) = 0.1$
 1082 and 0.3 m s^{-1} are shown in figures 11a,b respectively for $\mathcal{A}_h = 1 \text{ m}^2 \text{ s}^{-1}$. It is clear that
 1083 increasing $U(H)$ has a large effect on the wave field, with vertical velocities increased
 1084 throughout the domain and increased dominant vertical and horizontal wavelengths as $U(z)$
 1085 increases.

1086 As before, waves are generated at the topography in the range $|f| < |U(0)k| < |N|$. This
 1087 range can be visualised in figure 3b as the range of wavelengths for which the overlap
 1088 parameter γ is finite for $U = 0.1 \text{ m s}^{-1}$ (orange line). These are the only propagating
 1089 wavelengths that exist in the solution. However, as U increases with height to $U(H) =$
 1090 0.3 m s^{-1} , the range of wavenumbers that can propagate shifts to $|f| < |U(H)k| < |N|$,
 1091 shown in figure 3b as the range for which γ is finite for $U = 0.3 \text{ m s}^{-1}$ (magenta line).
 1092 Thus, wavenumbers k such that $|N|/|U(H)| < |k| < |N|/|U(0)|$ must reach their turning
 1093 levels and reflect downwards before reaching the surface. The waves that reach the surface
 1094 therefore have an increased minimum horizontal wavelength, as seen in figure 11b, and decay
 1095 more slowly as a result. Furthermore, the WKB solution (2.56) for waves that do not reach
 1096 turning levels showed (in the hydrostatic and non-rotating limit) that the viscous decay scale
 1097 $\sim U^2/\mathcal{A}_h N k$, thus as U increases the effect of viscosity is felt less by the waves. Equivalently,
 1098 the vertical group velocity of the waves increases with increasing U (shown for uniform U in
 1099 figure 4b), leading to less energy loss during propagation over a given vertical distance. The
 1100 reduced viscous decay results in increased interference between upwards and downwards
 1101 propagating waves (c.f. figure 9), shown in figure 12 as the shaded range becoming wider
 1102 with both increasing $U(H)$ and decreasing \mathcal{A}_h .

1103 The energy flux when $\mathcal{A}_h = 0.5 \text{ m}^2 \text{ s}^{-1}$ (figure 12a) is highly dependent on the choice of
 1104 depth H , and there is significant interference when $U(H) = 0.2$ and 0.3 m s^{-1} (shown by
 1105 the wide magenta and blue shaded areas). The bottom energy flux when $U(H) = 0.3 \text{ m s}^{-1}$
 1106 changes from 65 - 155% of its OB value (black dashed line) as H varies between 2900 and
 1107 3100 m, and this makes it difficult to compare the profiles of these solutions. However, the
 1108 energy flux when $\mathcal{A}_h = 1 \text{ m}^2 \text{ s}^{-1}$ (figure 12e) at all levels is greater when $U(H) = 0.2$ and
 1109 0.3 m s^{-1} than when U is uniform, except for near the topography when there is significant

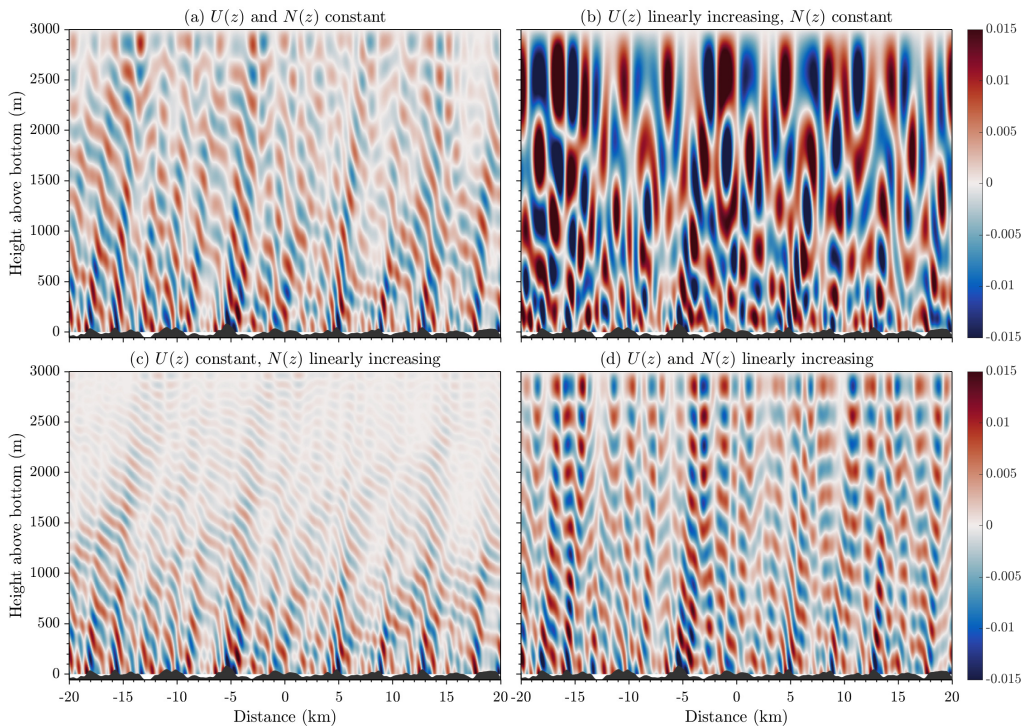


Figure 11: Vertical velocity (m s^{-1}) in the RL solver, with linear $U(z)$ and $N(z)$ with bottom values $U(0) = 0.1 \text{ m s}^{-1}$, $N(0) = 1 \times 10^{-3} \text{ s}^{-1}$, and (a) $U(H) = 0.1 \text{ m s}^{-1}$, $N(H) = 1 \times 10^{-3} \text{ s}^{-1}$ (b) $U(H) = 0.3 \text{ m s}^{-1}$, $N(H) = 1 \times 10^{-3} \text{ s}^{-1}$ (c) $U(H) = 0.1 \text{ m s}^{-1}$, $N(H) = 3 \times 10^{-3} \text{ s}^{-1}$ (d) $U(H) = 0.3 \text{ m s}^{-1}$, $N(H) = 3 \times 10^{-3} \text{ s}^{-1}$. $\mathcal{A}_h = 1 \text{ m}^2 \text{ s}^{-1}$, $\alpha = 1$, and $f = -1 \times 10^{-4} \text{ s}^{-1}$ in all cases. Topography $h(x)$ is shown, although it is applied in the linear approximation at its mean value of $z = 0$.

1110 destructive interference (blue shaded area). Aside from the ranges of the solutions (shaded),
 1111 there is not a large difference between the energy fluxes in the cases $U(H) = 0.2$ and
 1112 0.3 m s^{-1} , likely due to the effect of certain larger wavenumbers reaching their turning levels
 1113 at $|U(z)k| = |N|$ and reflecting before reaching the surface, decreasing upwards energy flux
 1114 at higher levels. From (2.49) and (2.50), the energy flux \overline{pw} is expected to increase with
 1115 increasing $U(z)$ when there is no energy loss and the E-P flux is conserved. However, the RL
 1116 solution constrains the energy flux to vanish at the surface, thus the convexity of the energy
 1117 flux in z will be determined by the balance between the gradient of the E-P flux due to energy
 1118 loss and reflection, and the gradient of $U(z)$.

1119 The most obvious result of increasing the velocity with height is the increase in the
 1120 RMS vertical velocity, shown in figures 12b,f. Despite the large ranges due to interference,
 1121 especially when $\mathcal{A}_h = 0.5 \text{ m}^2 \text{ s}^{-1}$, increasing $U(H)$ clearly increases w_{rms} over the whole
 1122 water column. This is consistent with the expected scaling from the WKB solution (2.56) and
 1123 figure 5b. When $\mathcal{A}_h = 1 \text{ m}^2 \text{ s}^{-1}$ and $U(H) = 0.3 \text{ m s}^{-1}$ (figure 12f, blue line), the subsurface
 1124 maximum is 4.5 times as large as that when $U(H) = 0.1 \text{ m s}^{-1}$ (black line), and over twice
 1125 as large as its bottom value. The vertical wavelength also clearly increases with increasing
 1126 U , as also seen in figure 11b.

1127 As discussed by Kunze & Lien (2019), lee waves can exchange energy with the mean
 1128 flow due to conservation of wave action E/kU , where E is the energy density (Bretherton

1129 & Garrett 1969). For a given wavenumber k , when there is no energy lost to dissipation,
 1130 the wave energy density will therefore increase with height when U increases with height.
 1131 Here, the energy lost to dissipation means that the wave action is not conserved, but we still
 1132 expect the wave energy to increase in the upper water column when $U(z)$ increases with
 1133 height compared to when $U(z)$ is constant. Energy loss would also be expected to increase
 1134 along with wave energy density for a given wavenumber. Similarly to the energy flux in
 1135 figure 12a, the large shaded areas in the energy loss in figure 12c due to interferences in the
 1136 case $\mathcal{A}_h = 0.5 \text{ m}^2 \text{ s}^{-1}$ make interpretation difficult. However, figure 12g for $\mathcal{A}_h = 1 \text{ m}^2 \text{ s}^{-1}$
 1137 demonstrates that energy loss over the water column does generally increase with increasing
 1138 $U(H)$. However, because energy at some wavenumbers no longer reaches the surface, having
 1139 reached the corresponding turning level at $|U(z)k| = |N|$, the increase in wave energy (and
 1140 energy loss) in the upper ocean is not as great for the multichromatic spectrum of waves as
 1141 for a single component that reaches the surface. The waves that do reach the surface also
 1142 experience less energy loss due to their larger horizontal scale.

1143 Although the energy loss is generally greater when U increases with z , figures 12d,h show
 1144 that the vertical gradient of the E-P flux is not, aside from the changes due to interference.
 1145 Since F is conserved when there is no mixing or dissipation, the flux does not increase due
 1146 to interaction with the shear. Neglecting wave interference from surface reflections at the
 1147 topography, the total wave drag $-\rho_0 F(0)$ depends only on the local bottom fields, and thus
 1148 remains constant with changes in U with height. However, the total mixing and dissipation
 1149 need not, since the waves can gain energy from the mean flow during propagation.

1150 We now consider the effect of increasing the stratification $N(z)$ on the lee waves in the RL
 1151 solver. The vertical velocity field is shown in figure 11c. The vertical wavelengths are clearly
 1152 reduced as N increases, since the vertical wavenumber $m \sim N/U$. The vertical velocities are
 1153 also reduced higher in the water column when compared to figure 11a. Figure 13 shows the
 1154 horizontally averaged vertical profiles as in figure 12. It is immediately clear from the lack of
 1155 shaded area that in the cases shown, constructive/ destructive interference does not greatly
 1156 affect the amplitude of the solutions, even for the lower value of \mathcal{A}_h , and to a decreasing
 1157 extent for increasing $N(H)$. This is because the vertical group velocity (2.40) scales as $1/N$,
 1158 so the waves slow down and lose more energy during their propagation and thus interact
 1159 less. If vertical viscosity and diffusivity were implemented, the smaller vertical wavelengths
 1160 associated with increased N would dissipate even more quickly.

1161 Figures 13b,f show that the effect of increasing N with height is to reduce the vertical
 1162 velocities, in agreement with the WKB solution (2.56). This is because increasing N when U
 1163 is fixed makes the waves more inertial (since the upper bound for the radiating wavenumber
 1164 range N/U is increased, while the lower bound f/U is fixed). Since varying N with height
 1165 does not affect the energy flux in the same way as changing the velocity does (c.f. (2.49)), the
 1166 other results in figure 13 are easily interpreted. The increase in energy loss associated with
 1167 reduced group velocity when N is increasing causes a reduction in energy flux (figure 13e,
 1168 less clear in figure 13a due to interference), and a skewing of energy loss (figures 13c,g) and
 1169 gradient of the E-P flux (figure 13d,h) towards the lower part of the domain. Note from (2.51)
 1170 that the vertically integrated energy loss for a given \mathcal{A}_h is constant with changing $N(H)$
 1171 (when $U(z)$ is constant), as is the total wave drag force on the flow, given by the integral of
 1172 F_z .

1173 Next, we present results for simultaneously varying $U(z)$ and $N(z)$, keeping their ratio
 1174 constant at $U(z) = 100 \times N(z)$, so that the vertical wavelengths of the lee wave field are
 1175 comparable to the uniform background case. This is a fairly realistic scenario for the ocean,
 1176 where both U and N can be expected to increase with height above bottom. Figure 11d shows
 1177 the vertical velocity field when both U and N triple between the bottom and the surface.
 1178 The vertical wavelengths are comparable with figure 11a as expected, however, the vertical

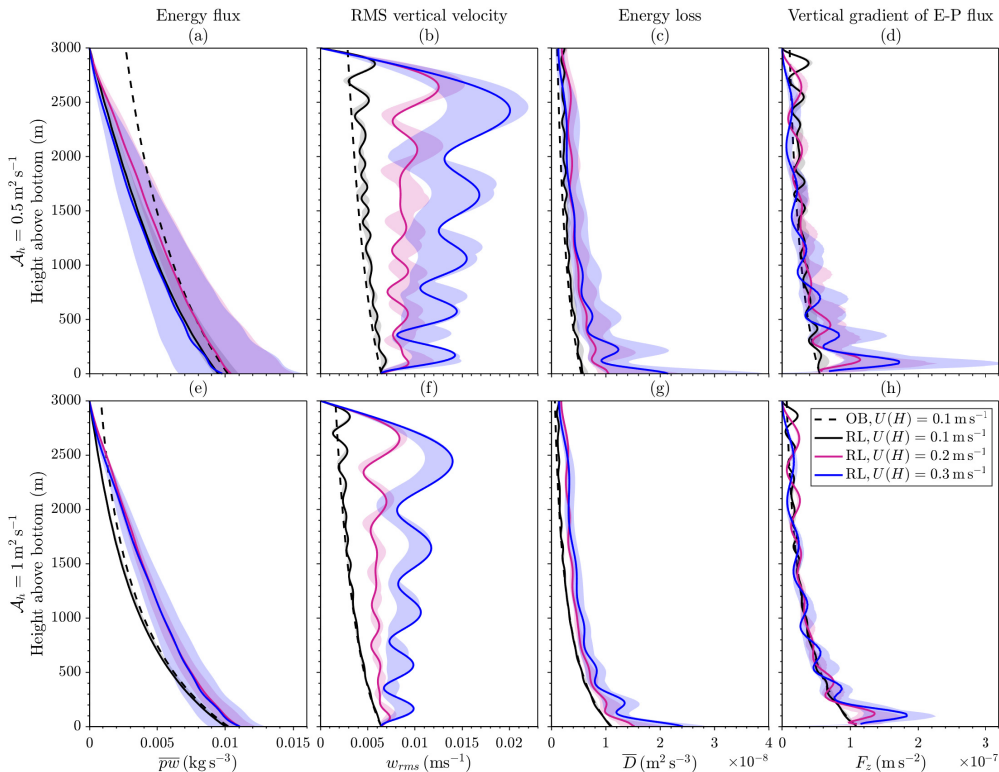


Figure 12: Same fields as figure 8, with $\mathcal{A}_h = 0.5 \text{ m}^2 \text{ s}^{-2}$ (top row) and $\mathcal{A}_h = 1 \text{ m}^2 \text{ s}^{-2}$ (bottom row). Solutions are for the nonhydrostatic and rotating case at various $U(H)$, where $U(z)$ is linear and $U(0) = 0.1 \text{ m s}^{-1}$. Shading as in figure 10, $f = -1 \times 10^{-4} \text{ s}^{-1}$, $N = 1 \times 10^{-3} \text{ s}^{-1}$.

1179 velocities are intensified, and there is more interference of the upwards and downwards
1180 propagating waves.

1181 The energy flux with height is shown in figures 14a,e for $\mathcal{A}_h = 0.5$ and $1 \text{ m}^2 \text{ s}^{-1}$
1182 respectively. As in figure 12, the ranges associated with interference are wider for larger $U(H)$
1183 and smaller \mathcal{A}_h . In general, upper ocean energy flux appears to increase with increasing $U(H)$
1184 and $N(H)$, although this isn't clear for $\mathcal{A}_h = 0.5 \text{ m}^2 \text{ s}^{-1}$ because of the significant interference.
1185 This is due to energy flux increasing when U increases with height (see (2.46) and (2.50)),
1186 without the impact of turning levels as in figure 12, since U/N remains constant. The gradient
1187 of the E-P flux (figures 14d,h), has a similar structure in the vertical for each case, with a
1188 greater range due to interference for larger $U(H)$ and smaller \mathcal{A}_h . The distribution of the
1189 forcing on the mean flow is therefore largely unchanged by increasing U and N with height.

1190 The upper ocean energy loss for $\mathcal{A}_h = 1 \text{ m}^2 \text{ s}^{-1}$ (figure 14g) increases with increasing
1191 $U(H)$ and $N(H)$, which can be explained as before by conservation of wave action as U
1192 increases, transferring energy to the wave field and increasing the wave energy density and
1193 hence energy loss. However, unlike the U increasing case (figure 12c), the energy loss at most
1194 heights is now strictly increasing with $U(H)$, since the constant ratio of U/N means that the
1195 range of radiating wavenumbers does not change with height, thus no wavenumber reaches
1196 a turning level. The result of this is that the energy loss in the upper ocean is significantly
1197 enhanced when U and N increase with height. The energy loss in the upper 1000 m is three
1198 times larger when U and N approximately triple with height than when they are uniform

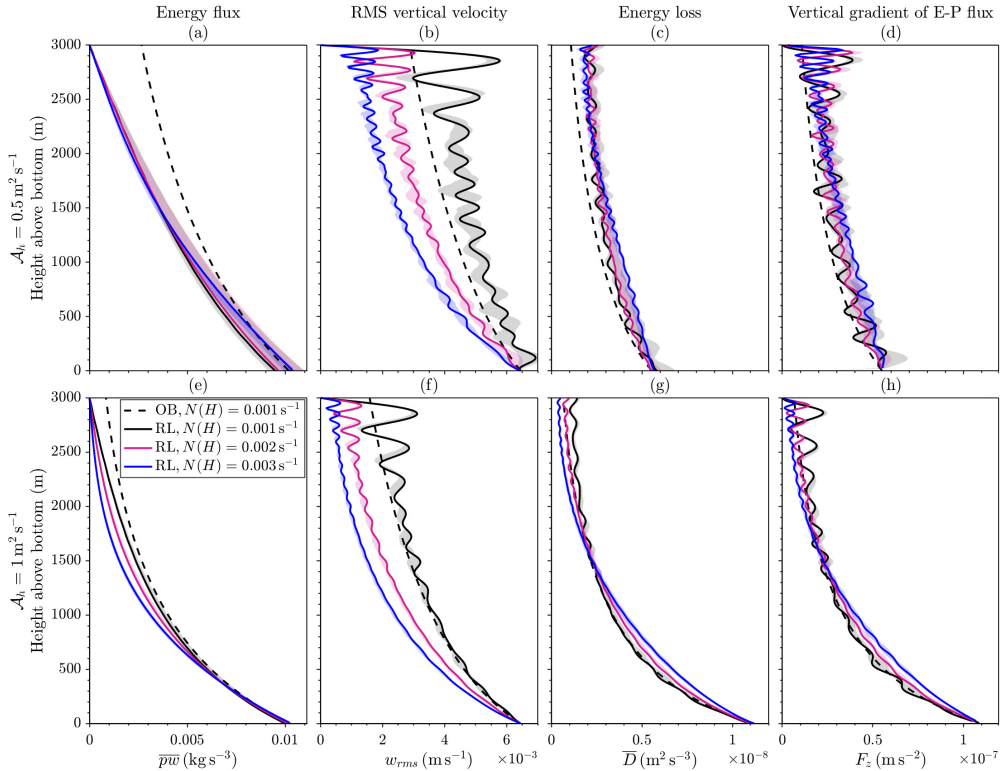


Figure 13: Same fields as figure 8, with $\mathcal{A}_h = 0.5 \text{ m}^2 \text{ s}^{-2}$ (top row) and $\mathcal{A}_h = 1 \text{ m}^2 \text{ s}^{-2}$ (bottom row). Solutions are for the nonhydrostatic and rotating case at various $N(H)$, where $N(z)$ is linear and $N(0) = 1 \times 10^{-3} \text{ s}^{-1}$. Shading as in figure 10, $f = -1 \times 10^{-4} \text{ s}^{-1}$, $U = 0.1 \text{ m s}^{-1}$.

1199 throughout the water column (both with a RL and $H = 3000 \text{ m}$). For the lower viscosity
 1200 value $\mathcal{A}_h = 0.5 \text{ m}^2 \text{ s}^{-1}$ (figure 14c), the wide shaded regions due to interference make this
 1201 result less clear, but the constructive interference allows the energy loss in the upper 1000 m
 1202 for $U(H) = 0.3 \text{ m s}^{-1}$ to be up to ~ 6 times as large as in the OB case.

1203 The change in energy loss with height for the various background flows with $\mathcal{A}_h = 1 \text{ m}^2 \text{ s}^{-1}$
 1204 is also illustrated in figure 15. As we have seen, energy loss increases slightly with height
 1205 with respect to the uniform fields when U increases with height, and decreases when N
 1206 increases with height. The combination of increasing both U and N , however, allows the
 1207 waves to stay in their radiating range and gives the maximum upper ocean energy loss.

1208 Another interesting result is the large increase in RMS vertical velocity with height when U
 1209 and N increase together (figures 14b,f), suggesting that the increase of w_{rms} due to increasing
 1210 U is dominant over the decrease in w_{rms} due to increasing N (see figures 12b,f and 13b,f).
 1211 This is consistent with the WKB solution (2.56) and figure 5d, and as discussed in §2.11 is
 1212 because of reduced energy loss due to the increased viscous decay scale, or equivalently the
 1213 increased vertical group velocity, compared to the uniform background case. The subsurface
 1214 maximum of w_{rms} when $U(H) = 0.3 \text{ m s}^{-1}$ and $\mathcal{A}_h = 1 \text{ m}^2 \text{ s}^{-1}$ is twice as large as that
 1215 when $U(H) = 0.1 \text{ m s}^{-1}$, and nearly 4 times as large as w_{rms} in the OB solution at the same
 1216 height. The impact of the boundary is substantial, with the variation in w_{rms} over a vertical
 1217 wavelength due to superposition increasing with increasing $U(H)$ and $N(H)$.

1218 Finally, we consider the effect of a more realistic stratification in the upper ocean.

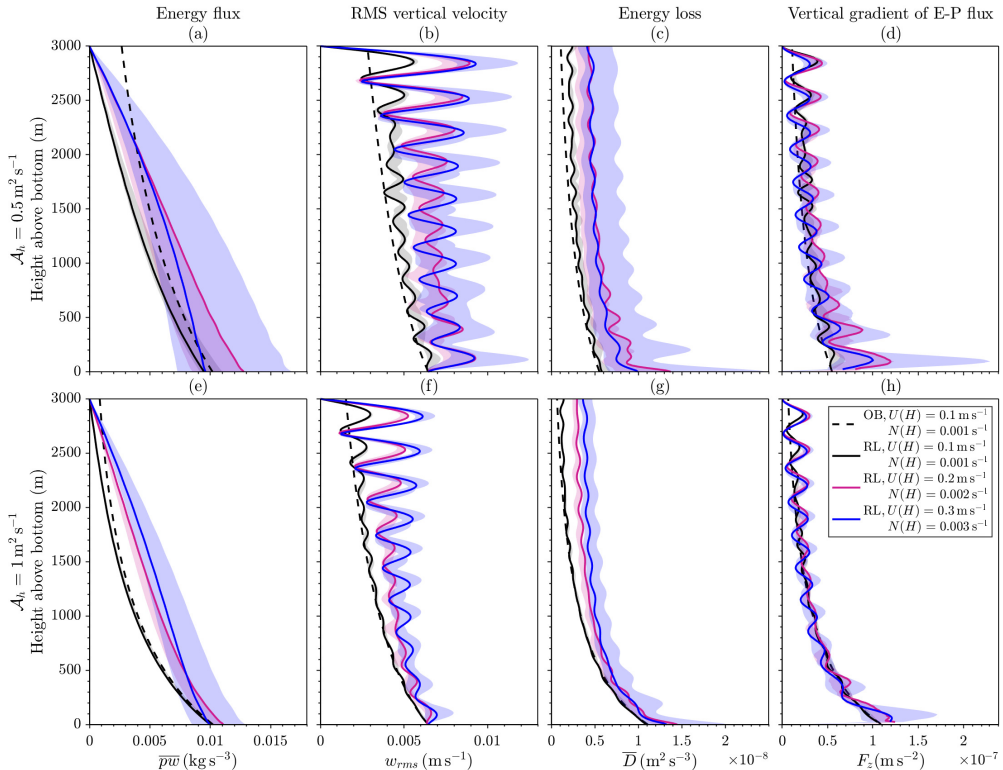


Figure 14: Same fields as figure 8, with $\mathcal{A}_h = 0.5 \text{ m}^2 \text{ s}^{-2}$ (top row) and $\mathcal{A}_h = 1 \text{ m}^2 \text{ s}^{-2}$ (bottom row). Solutions are for the nonhydrostatic and rotating case at various $U(H)$, where $U(H)$ is linear and $U(H) = 100N(H)$. Shading as in figure 10, $f = -1 \times 10^{-4} \text{ s}^{-1}$.

1219 Typically, there exists a maximum of stratification at the thermocline, and a mixed layer
 1220 at the surface where stratification is near zero. We use a simplified example stratification
 1221 representative of the mean stratification in realistic Drake Passage simulations (which are
 1222 themselves constrained by observed hydrographic information), having a maximum at around
 1223 500 m depth and decreasing to zero at the surface (Mashayek *et al.* 2017). In reality, the
 1224 stratification can have a second sharp maximum below the thin surface mixed layer dependent
 1225 on seasonality, but the deeper thermocline is a persistent feature. For comparison with the
 1226 previous experiments, N is linear (and N^2 quadratic) at depth, and modified using a tanh
 1227 function to create the thermocline. Figure 16a shows the profiles of N^2 used, U is linearly
 1228 increasing from $U(0) = 0.1$ to $U(H) = 0.3 \text{ m s}^{-1}$, and $\mathcal{A}_h = 1 \text{ m}^2 \text{ s}^{-2}$. The effect of the
 1229 drop in stratification at the surface, as might be expected from figures 13b,f, is to further
 1230 enhance the subsurface peak in RMS vertical velocity (figure 16b). Although w_{rms} increases,
 1231 the buoyancy and horizontal velocity perturbations decrease with N^2 near the surface (not
 1232 shown), leading to a decrease in total flow energy and energy loss (figure 16c). The combined
 1233 effect of increasing velocity with height above bottom, the reflecting upper boundary, and a
 1234 near surface decrease in stratification all act to increase the subsurface peak in RMS vertical
 1235 velocity.

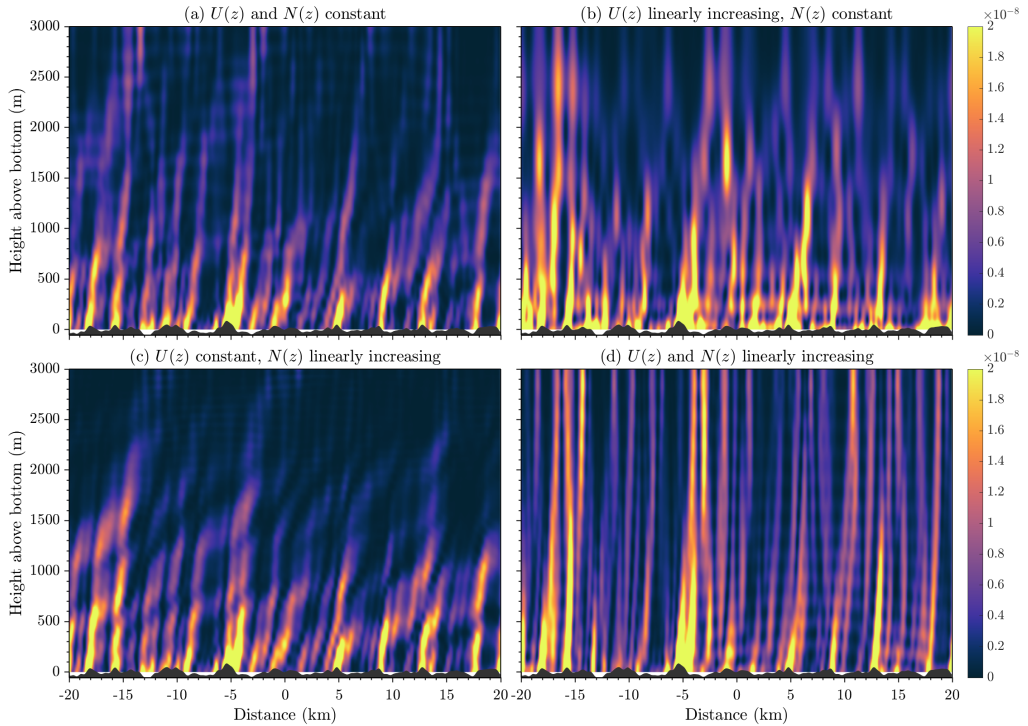


Figure 15: Energy loss D ($\text{m}^2 \text{s}^{-3}$) in the RL solver, with the same mean flow and parameters described in figure 11.

1236 5. Conclusions

1237 Lee waves generated by stratified geostrophic flow over topography play an important role
 1238 in the buoyancy and momentum budgets of the ocean, causing diapycnal mixing and drag
 1239 on the mean flow when they break. Occurring at the sub-gridscale of global models, they
 1240 require parametrisation to represent their effect on the mean flow.

1241 Linear theory with constant background velocity and stratification and a radiating upper
 1242 boundary has often been used to predict the generation rate of lee waves. However, although
 1243 this approximation may be sufficient locally to estimate the generation of lee waves, it does
 1244 not allow any deductions on their propagation throughout the water column and eventual
 1245 dissipation or re-absorption to the mean flow. The mean velocity and stratification in typical
 1246 oceanic flows varies by up to an order of magnitude between the abyssal ocean and the
 1247 surface, and the ocean surface is poorly represented by a radiating boundary condition,
 1248 instead acting to reflect incident lee waves.

1249 Motivated by high resolution realistic simulations of the Drake Passage, a region of high
 1250 lee wave generation, we developed a theory for lee waves with an air-sea boundary, variable
 1251 background velocity and stratification, and a representation of energy lost to dissipation and
 1252 mixing. The structures observed in the simulations agree qualitatively with our theoretical
 1253 predictions, and reconciling the two will be the subject of a follow up study.

1254 We find that allowing lee waves to reflect at the surface has the potential to substantially
 1255 modify the lee wave field, increasing vertical velocities and mixing and dissipation, especially
 1256 in the upper ocean where shear and stratification are typically enhanced.

1257 Allowing waves to reflect at the surface allows interference between the upwards and
 1258 downwards propagating components, and this can modify the lee wave generation itself.

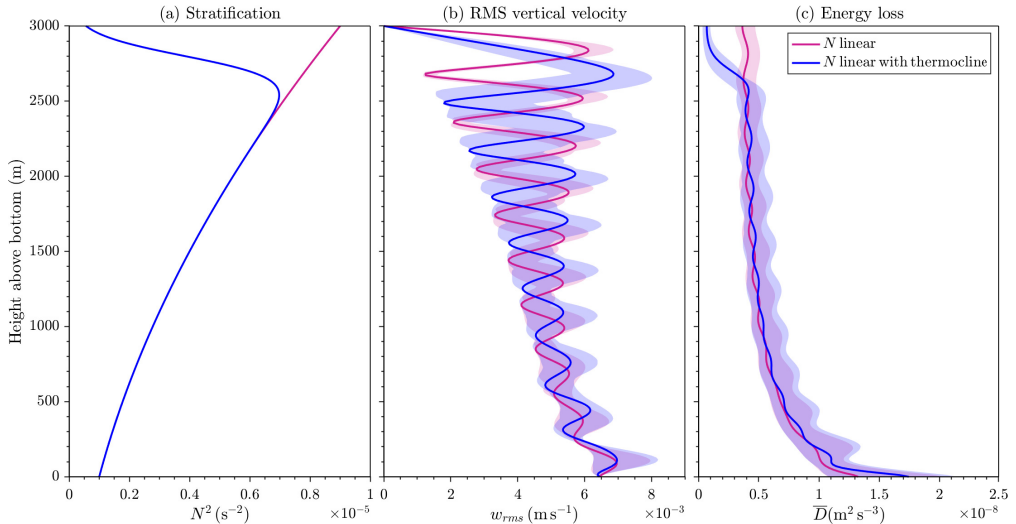


Figure 16: (a) Stratification, (b) RMS vertical velocity, and (c) energy loss as a function of z for the RL solver. U is linear with $U(z) = 0.1(1 + 2z/H)$. The linear N profile is $N(z) = 0.001(1 + 2z/H)$, and with the thermocline included is $N(z) = 0.001(1 + 2z/H)\sqrt{(1 + \tanh(18 - 20z/H))/(1 + \tanh(18))}$. Results from the RL solver are shown as a range (shaded) of solutions with $H = 2900$ to 3100 m (with axes scaled onto $z \in [0, 3000]$ m) to show the effect of constructive/destructive interference, and in solid at for $H = 3000$ m. $\mathcal{A}_h = 1 \text{ m}^2 \text{ s}^{-1}$, $f = -1 \times 10^{-4} \text{ s}^{-1}$.

1259 Under certain conditions, this may manifest as a resonance of the system - although rotation
 1260 and non-hydrostaticity act to lessen this effect.

1261 The upper boundary alone acts to enhance near surface vertical velocities, and shift the
 1262 energy loss of the lee wave field higher in the water column. However, the impact of our
 1263 full water column view of lee waves is most significant when combined with non-uniform
 1264 background flows, as are typical of realistic ocean conditions.

1265 When the background velocity increases with height above the sea floor, as is often the
 1266 case in wind driven geostrophic flows, we find that the impact of the reflection from the
 1267 surface increases and that the lee wave vertical velocities are significantly enhanced in
 1268 the upper ocean. The lee wave drag is largely unchanged, but the energy in the lee wave
 1269 field, and hence the energy lost to mixing and dissipation, increases since energy transfers
 1270 from the sheared mean flow to the waves. If the stratification also increases with height
 1271 such that U/N remains fairly constant, the waves that are generated at topography are all
 1272 able to reach the surface, increasing the upper ocean wave energy and energy loss. The
 1273 inclusion of a weakly stratified surface mixed layer acts to enhance near surface vertical
 1274 velocities further, and reduces near surface energy loss. Therefore, parametrising the effect
 1275 of lee waves propagating through changing background flows may be essential for correctly
 1276 estimating their impact on mixing.

1277 The simplifications made in this study leave some questions as to the applicability of
 1278 these results to the real ocean. In particular, although linear lee wave approximations have
 1279 been shown to give good agreement with nonlinear simulations under certain conditions,
 1280 the wave interactions discussed here that cause modification to wave drag and energy flux
 1281 could be significantly altered by nonlinear topography. The assumption of linearity also has
 1282 consequences for the wave-mean flow interaction, particularly when the background flow
 1283 changes with height and energy transfers between waves and mean flow. Here, the mean flow

1284 is forced to remain constant, whereas in practise the mean flow would lose energy to the lee
1285 waves.

1286 The contribution of time dependent components of the background flow, including tides,
1287 could change the nature of the wave generation and interactions. The coupling between
1288 internal tide and lee wave generation has recently been suggested to significantly affect
1289 lee wave generation rates, reducing global estimates of lee wave energy flux by 13-19%
1290 (Shakespeare 2020; Dossmann *et al.* 2020). The unsteady nature of tides themselves could
1291 also impact the lee wave reflection and superposition through modification of the large scale
1292 flow. Further studies are needed to quantify the impact of tidal flows on the mechanisms
1293 discussed here.

1294 The constructive and destructive interference of the wave field may be overestimated due
1295 to the use of a periodic topography consisting of a finite sum of topographic components.
1296 It is likely that for a realistic topography, where the peaks of topography that generate lee
1297 waves are isolated and at different heights, this effect is substantially reduced. The effect
1298 of 3D topography could also alter the results, and this could be investigated in the linear
1299 framework by extending the solver.

1300 We implemented a horizontal viscosity and diffusivity in place of the full Laplacian
1301 parametrisation of lee wave energy loss for mathematical simplicity, which becomes unreal-
1302 istic when the vertical scale of lee waves changes substantially over the depth of the water
1303 column. Breaking due to instabilities of the lee waves themselves is not explicitly accounted
1304 for, since the viscosity and diffusivity are constant with height. The appropriate values of
1305 viscosity and diffusivity should also vary with the nonlinearity of the waves themselves,
1306 and this could be especially important when the background flow changes with height,
1307 potentially changing the stability of the waves. The theory could be extended to allow a more
1308 realistic and vertically varying viscosity profile in a future work. However, using this simple
1309 parametrisation, the resulting energy loss can be tuned to agree with results from previous
1310 nonlinear simulations with similar topography and background flow (Nikurashin & Ferrari
1311 2010*b*).

1312 A rigid lid boundary condition has been used here, justified by the lack of impact of a free
1313 surface on the structure of the waves in the interior. However, predictions of the sea surface
1314 height imprint of these waves could be made within our theory. This could perhaps eventually
1315 allow observational diagnostics - modern satellite observations are fast approaching the
1316 $O(1\text{ km})$ horizontal resolution and $O(1\text{ cm})$ precision that would be necessary to detect the
1317 very largest waves (Neeck *et al.* 2012). Satellite sun glitter images can also qualitatively be
1318 used to diagnose lee wave surface signatures (de Marez *et al.* 2020). The rigid lid condition
1319 would however be appropriate for modelling under-ice lee waves, whose surface normal
1320 stress could play a role in sea ice or ice shelf dynamics.

1321 The results of this study indicate that the reflection of lee waves at the ocean surface and
1322 their presence in the upper ocean cannot always be neglected, especially when the mean
1323 flow is surface intensified. Climate model parametrisations may need to take into account
1324 the impact of changing background mean flows and surface reflections in order to correctly
1325 estimate the vertical structure of mixing and dissipation. Enhanced upper ocean mixing could
1326 have important consequences for tracer transport between the surface and interior ocean. The
1327 dynamics of the near surface wave field and its interaction with surface submesoscales should
1328 also be investigated further, since the horizontal lengthscales are very similar. Further studies
1329 will aim to verify the theory developed here against realistic nonlinear simulations, and
1330 investigate the impact of these waves on surface processes.

1331 **Acknowledgments**

1332 The authors are grateful to Callum Shakespeare and two other anonymous reviewers of
 1333 the manuscript for their helpful and constructive comments. L.B. was supported by the
 1334 Centre for Doctoral Training in Mathematics of Planet Earth, UK EPSRC funded (grant
 1335 no. EP/L016613/1), and A.M. acknowledges funding from the NERC IRF fellowship grant
 1336 NE/P018319/1.

1337

1338 Declaration of Interests. The authors report no conflict of interest.

REFERENCES

- 1339 ANDREWS, D. G. & MCINTYRE, M. E. 1976 Planetary Waves in Horizontal and Vertical Shear: The
 1340 Generalized Eliassen-Palm Relation and the Mean Zonal Acceleration. *J. Atmos. Sci.* **33** (11).
- 1341 BACHMAN, S. D., TAYLOR, J. R., ADAMS, K. A. & HOSEGOOD, P. J. 2017 Mesoscale and submesoscale effects
 1342 on mixed layer depth in the Southern Ocean. *J. Phys. Oceanogr.* **47** (9), 2173–2188.
- 1343 BAINES, P. G. 1995 *Topographic effects in stratified flows*. Cambridge University Press.
- 1344 BELL, T. H. 1975 Topographically generated internal waves in the open ocean. *J. Geophys. Res.* **80** (3),
 1345 320–327.
- 1346 BOOKER, J. R. & BRETHERTON, F. P. 1967 The critical layer for internal gravity waves in a shear flow. *J.*
 1347 *Fluid Mech.* **27** (3), 513–539.
- 1348 BREARLEY, J. A., SHEEN, K. L., NAVEIRA GARABATO, A. C., SMEED, D. A. & WATERMAN, S. 2013 Eddy-
 1349 induced modulation of turbulent dissipation over rough topography in the Southern Ocean. *J. Phys.*
 1350 *Oceanogr.* **43** (11), 2288–2308.
- 1351 BRETHERTON, F. P. 1969 Momentum transport by gravity waves. *Q. J. R. Meteorol. Soc.* **95**, 125–135.
- 1352 BRETHERTON, F. P. & GARRETT, C. 1969 Wavetrains in inhomogeneous moving media. *Proc. R. Soc. A* **302**,
 1353 529–554.
- 1354 CESSI, P. 2019 The global overturning circulation *Annu. Rev. Mar. Sci.* **11** 249–270.
- 1355 CHARNEY, J. G., DRAZIN, P. G. 1961 Propagation of planetary-scale disturbances from the lower into the
 1356 upper atmosphere *J. Geophys. Res.* **66** 83–109.
- 1357 CIMOLI, L., ET AL 2021 Significance of diapycnal mixing within the Atlantic Meridional Overturning
 1358 Circulation *Nat. Commun.* (under review).
- 1359 CUSACK, J. M., NAVEIRA GARABATO, A. C., SMEED, D. A. & GIRTON, J. B. 2017 Observation of a Large Lee
 1360 Wave in the Drake Passage. *J. Phys. Oceanogr.* **47** (4), 793–810.
- 1361 CUSACK, J. M., BREARLEY, J. A., NAVEIRA GARABATO, A. C., SMEED, D. A., POLZIN, K. L., VELZEBOER,
 1362 N. & SHAKESPEARE, C. J. 2020 Observed eddy-internal wave interactions in the Southern Ocean. *J.*
 1363 *Phys. Oceanogr.* **50**, 3043–3062.
- 1364 DOSSMANN, Y., SHAKESPEARE, C., STEWART, K. & HOGG, A. 2020 Asymmetric internal tide generation in
 1365 the presence of a steady flow. *J. Geophys. Res. Ocean.* **125**.
- 1366 ELIASSEN, A. & PALM, E. 1960 On the Transfer of Energy in Stationary Mountain Waves. *Geophys. Nor.*
 1367 **XXII** (3), 1–23.
- 1368 FOX-KEMPER, B. & MENEMENLIS, D. 2008 Can large eddy simulation techniques improve mesoscale rich
 1369 ocean models? *Geophys. Monogr. Ser.* **177**, 319–337.
- 1370 GILL, A. E. 1982 *Atmosphere-Ocean Dynamics*. Academic Press.
- 1371 GOFF, J. A. & JORDAN, T. H. 1988 Stochastic Modeling of Seafloor Morphology. *J. Geophys. Res.* **93**.
- 1372 GRIMSHAW, R. 1975 Internal gravity waves: Critical layer absorption in a rotating fluid. *J. Fluid Mech.* **70** (2),
 1373 287–304.
- 1374 JONES, W. L. 1967 Propagation of internal gravity waves in fluids with shear flow and rotation. *J. Fluid*
 1375 *Mech.* **30** (3), 439–448.
- 1376 KLYMAK, J. M. 2018 Nonpropagating form drag and turbulence due to stratified flow over large-scale Abyssal
 1377 Hill Topography. *J. Phys. Oceanogr.* **48** (10), 2383–2395.
- 1378 KUNZE, E. & LIEN, R. C. 2019 Energy Sinks for Lee Waves in Shear Flow. *J. Phys. Oceanogr.* 2851–2865.
- 1379 LARGE, W. G., MCWILLIAMS, J. C. & DONEY, S. C. 1994 Oceanic vertical mixing: A review and a model
 1380 with a nonlocal boundary layer parameterization. *Rev. Geophys.* **32** (4), 363–403.
- 1381 LEGG, S. 2021 Mixing by Oceanic Lee Waves *Annu. Rev. Fluid Mech.* 173–201.
- 1382 LEITH, C. E. 1996 Stochastic models of chaotic systems. *Phys. D Nonlinear Phenom.* **98** (2-4), 481–491.

- 1383 MACKINNON, J. A., ET AL 2017 Climate Process Team on Internal Wave–Driven Ocean Mixing. *Bull. Am.*
1384 *Meteorol. Soc.* **98** (11), 2429–2454.
- 1385 DE MAREZ, C., LAHAYE, N. & GULA, J. 2020 Interaction of the Gulf Stream with small scale topography: a
1386 focus on lee waves. *Sci. Rep.* **10** (2332).
- 1387 MARSHALL, J., ADCROFT, A., HILL, C., PERELMAN, L. & HEISEY, C. 1997 A finite-volume, incompressible
1388 Navier Stokes model for studies of the ocean on parallel computers. *J. Geophys. Res.* **102** (C3),
1389 5753–5766.
- 1390 MASHAYEK, A., FERRARI, R., MERRIFIELD, S., LEDWELL, J. R., ST LAURENT, L. & NAVEIRA GARABATO, A.
1391 2017 Topographic enhancement of vertical turbulent mixing in the Southern Ocean. *Nat. Commun.*
1392 **8**, 1–12.
- 1393 MAYER, F. T. & FRINGER, O. B. 2017 An unambiguous definition of the Froude number for lee waves in the
1394 deep ocean. *J. Fluid Mech.* **831**, 1–9.
- 1395 MCINTYRE, M. E. 1972 On Long’s hypothesis of no upstream influence in uniformly stratified or rotating
1396 flow. *J. Fluid Mech.* **52** (2), 209–243.
- 1397 MELET, A., HALLBERG, R., LEGG, S. & NIKURASHIN, M. 2014 Sensitivity of the Ocean State to Lee
1398 Wave–Driven Mixing. *J. Phys. Oceanogr.* **44** (3), 900–921.
- 1399 NAVEIRA GARABATO, A. C., POLZIN, K. L., KING, B. A., HEYWOOD, K. J. & VISBECK, M. H. 2004 Mixing
1400 in the Southern Ocean. *Science* **303** (January), 210–213.
- 1401 NAVEIRA GARABATO, A. C., NURSER, A. J., SCOTT, R. B., & GOFF, J. A. 2013 The impact of small-scale
1402 topography on the dynamical balance of the ocean. *J. Phys. Oceanogr.* **43**, 647–668.
- 1403 NEECK, S. P., LINDSTROM, E. J., VAZE, P. V. & FU, L. L. 2012 Surface Water and Ocean Topography (SWOT)
1404 mission. *Sensors, Syst. Next-Generation Satell. XVI* **8533** (November 2012), 85330G.
- 1405 NIKURASHIN, M. & FERRARI, R. 2010a Radiation and Dissipation of Internal Waves Generated by
1406 Geostrophic Motions Impinging on Small-Scale Topography: Application to the Southern Ocean. *J.*
1407 *Phys. Oceanogr.* **40** (9), 2025–2042.
- 1408 NIKURASHIN, M. & FERRARI, R. 2010b Radiation and Dissipation of Internal Waves Generated by
1409 Geostrophic Motions Impinging on Small-Scale Topography: Theory. *J. Phys. Oceanogr.* **40**, 1055–
1410 1074.
- 1411 NIKURASHIN, M. & FERRARI, R. 2011 Global energy conversion rate from geostrophic flows into internal
1412 lee waves in the deep ocean. *Geophys. Res. Lett.* **38** (8), 1–6.
- 1413 NIKURASHIN, M. & FERRARI, R. 2013 Overturning circulation driven by breaking internal waves in the deep
1414 ocean. *Geophys. Res. Lett.* **40** (12), 3133–3137.
- 1415 NIKURASHIN, M., FERRARI, R., GRISOUARD, N. & POLZIN, K. 2014 The Impact of Finite-Amplitude Bottom
1416 Topography on Internal Wave Generation in the Southern Ocean. *J. Phys. Oceanogr.* **44** (11), 2938–
1417 2950.
- 1418 NIKURASHIN, M., VALLIS, G. K. & ADCROFT, A. 2012 Routes to energy dissipation for geostrophic flows in
1419 the Southern Ocean. *Nat. Geosci.* **6** (1), 48–51.
- 1420 PELTIER, W. & CLARK, T. 1979 The Evolution and Stability of Finite-Amplitude Mountain Waves. Part II:
1421 Surface Wave Drag and Severe Downslope Windstorms. *J. Atmos. Sci.*
- 1422 ROSSO, I., HOGG, A. M., KISS, A. E. & GAYEN, B. 2015 Topographic influence on submesoscale dynamics
1423 in the Southern Ocean. *Geophys. Res. Lett.* **42** (4), 1139–1147.
- 1424 SCORER, R. S. 1949 Theory of waves in the lee of mountains. *Q. J. R. Meteorol. Soc.* **75**, 41–56.
- 1425 SCOTT, R. B., GOFF, J. A., NAVEIRA GARABATO, A. C. & NURSER, A. J. 2011 Global rate and spectral
1426 characteristics of internal gravity wave generation by geostrophic flow over topography. *J. Geophys.*
1427 *Res.* **116** (C09029), 1–14.
- 1428 SHAKESPEARE, C. J. 2020 Interdependence of internal tide and lee wave generation at abyssal hills: Global
1429 calculations. *J. Phys. Oceanogr.* **50** (3), 655–677.
- 1430 SHAKESPEARE, C. J. & HOGG, A. M. 2017 The viscous lee wave problem and its implications for ocean
1431 modelling. *Ocean Model.* **113**, 22–29.
- 1432 SHEEN, K. L., ET AL 2013 Rates and mechanisms of turbulent dissipation and mixing in the Southern Ocean:
1433 Results from the Diapycnal and Isopycnal Mixing Experiment in the Southern Ocean (DIMES). *J.*
1434 *Geophys. Res. Ocean.* **118** (6), 2774–2792.
- 1435 SMITH, R. B. 1989 Mountain-induced stagnation points in hydrostatic flow. *Tellus A* **41 A** (3), 270–274.
- 1436 ST. LAURENT, L. C., SIMMONS, H. L. & JAYNE, S. R. 2002 Estimating tidally driven mixing in the deep ocean.
1437 *Geophys. Res. Lett.* **29** (23), 19–22.
- 1438 MASLOWE, S. 1986 Critical Layers in Shear Flows. *Annu. Rev. Fluid Mech.* **18**, 405–432.

- 1439 TALLEY, L., ET AL 2016 Changes in Ocean Heat, Carbon Content, and Ventilation: A Review of the First
1440 Decade of GO-SHIP Global Repeat Hydrography. *Annu. Rev. Mar. Sci.* **8**, 185–215.
- 1441 TEIXEIRA, M. A. C. 2014 The physics of orographic gravity wave drag. *Front. Phys.* **2**, 1–24.
- 1442 TEIXEIRA, M. A. C., ARGAIN, J. L. & MIRANDA, P. M. A. 2013 Orographic drag associated with lee waves
1443 trapped at an inversion. *J. Atmos. Sci.* **70** (9), 2930–2947.
- 1444 TEIXEIRA, M. A. C., MIRANDA, P. M. A., ARGAIN, J. L. & VALENTE, M. A. 2005 Resonant gravity-wave drag
1445 enhancement in linear stratified flow over mountains. *Q. J. R. Meteorol. Soc.* **131** (609), 1795–1814.
- 1446 WATERMAN, S., NAVEIRA GARABATO, A. C. & POLZIN, K. L. 2013 Internal waves and turbulence in the
1447 antarctic circumpolar current. *J. Phys. Oceanogr.* **43** (2), 259–282.
- 1448 WATERMAN, S., POLZIN, K. L., NAVEIRA GARABATO, A. C., SHEEN, K. L. & FORRYAN, A. 2014 Suppression
1449 of internal wave breaking in the antarctic circumpolar current near topography. *J. Phys. Oceanogr.*
1450 **44** (5), 1466–1492.
- 1451 WINTERS, K. B. & ARMI, L. 2012 Hydraulic control of continuously stratified flow over an obstacle. *J. Fluid*
1452 *Mech.* **700**, 502–513.
- 1453 WRIGHT, C. J., SCOTT, R. B., AILLIOT, P. & FURNIVAL, D. 2014 Lee wave generation rates in the deep ocean.
1454 *Geophys. Res. Lett.* **41** (7), 2434–2440.
- 1455 WURTELE, M. G. 1996 Atmospheric Lee Waves. *Annu. Rev. Fluid Mech.* **28** (1), 429–476.
- 1456 WURTELE, M. G., DATTA, A. & SHARMAN, R. D. 1996 The propagation of gravity-inertia waves and lee
1457 waves under a critical level *J. Atmos. Sci.*
- 1458 YANG, L., NIKURASHIN, M., HOGG, A. M. & SLOYAN, B. M. 2018 Energy Loss from Transient Eddies due
1459 to Lee Wave Generation in the Southern Ocean. *J. Phys. Oceanogr.* **48** (12), 2867–2885.
- 1460 ZHENG, K. & NIKURASHIN, M. 2019 Downstream Propagation and Remote Dissipation of Internal Waves in
1461 the Southern Ocean. *J. Phys. Oceanogr.*
- 1462 ZHENG, Q., HOLT, B., LI, X., LIU, X., ZHAO, Q., YUAN, Y. & YANG, X. 2012 Deep-water seamount wakes
1463 on SEASAT SAR image in the Gulf Stream region. *Geophys. Res. Lett.* **39**.